# Highly Efficient Thermo-Optic Switches on Silicon-On-Insulator

by

Kyle Murray

B. Eng., McMaster University, 2013

A THESIS SUBMITTED IN PARTIAL FULFILLMENT
OF THE REQUIREMENTS FOR THE DEGREE OF

**Master of Applied Science**

in

THE FACULTY OF GRADUATE AND POSTDOCTORAL STUDIES
(Electrical and Computer Engineering)

The University of British Columbia
(Vancouver)

August 2015

# Abstract

We analyze and demonstrate the performance of dense dissimilar waveguide routing as a method for increasing the efficiency of thermo-optic phase shifters on a silicon-on-insulator platform. Optical, mechanical, and thermal models of the phase shifters are developed and used to propose metrics for evaluating device performance. The lack of cross-coupling between dissimilar waveguides allows highly dense waveguide routing under heating elements and a corresponding increase in efficiency. We demonstrate a device with highly dense routing of 9 waveguides under a 10 $\mu$m wide heater and, by thermally isolating the phase shifter by removal of the silicon substrate, achieve a low switching power of 95 $\mu$W, extinction ratio greater than 20 dB, and less than 0.1 dB ripple in the through spectrum. The device has a footprint of less than 800 $\mu$m $\times$ 180 $\mu$m. The increase in waveguide density achieved by using dissimilar waveguide routing is found not to negatively impact the switch response time.

# Preface

I am the main author of the Optics Express journal paper titled "Dense dissimilar waveguide routing for highly efficient thermo-optic switches on silicon" [1], a coauthor of the submitted journal paper titled "Michelson interferometer thermo-optic switch on SOI with a 50 microwatt power consumption" [2], and a contributor to Chapter 4.1 of the book titled "Silicon Photonics Design: From Devices to Systems" [3].

My supervisor, Dr. Lukas Chrostowski, requested I perform simulations of dissimilar waveguide coupling to appear in [3], and the model and calculation methods that I developed to perform these simulations were later expanded into the coupled mode model of light propagation in folded waveguides that appears in [1] and Section 2.2 of this thesis.

I conceived the idea of utilizing dissimilar waveguide routing to increase the efficiency of thermo-optic phase shifters, developed models of the devices, designed the devices, measured the performance of the devices, and wrote the Optics Express paper. This work is the basis of the paper [1], and appears in Chapter 1, Section 2.2, and in Chapters 3 and 4 of this thesis. H. Jayatilleka assisted with the layout of the folded waveguide structures. H. Jayatilleka and Z. Lu assisted with editing of [1].

Z. Lu is the main author of the paper [2], for which I provided simulations of dissimilar waveguide coupling, advice on the design of the folded waveguides, and editing of the draft. The thermal simulations in [2], performed by Z. Lu, were expanded upon by myself to form Section 2.4 of this thesis.

Dr. Lukas Chrostowski guided my research by encouraging further exploration of dissimilar waveguide routing, by providing insight in to the design and meaurement of devices, and by editing drafts of the publications and of this thesis.

The following is a copyright notice regarding the content reproduced from [1]:



The complete list of publications are:

[1] K. Murray, Z. Lu, H. Jayatilleka, and L. Chrostowski, "Dense dissimilar waveguide routing for highly efficient thermo-optic switches on silicon," Opt. Express 23, 1957519585 (2015).
[2] Z. Lu, K. Murray, H. Jayatilleka, and L. Chrostowski, "Michelson interferometer thermo-optic switch on SOI with a 50 microwatt power consumption," Photon. Technol. Lett., IEEE pp. 11 (2015).
[3] L. Chrostowski and M. Hochberg, Silicon Photonics Design: From Devices to Systems (Cambridge University Press, 2015). Chap. 4.1.

# Table of Contents

# List of Tables

# List of Figures

# Glossary

**SOI** silicon-on-insulator

**MZI** Mach-Zehnder interferometer

**CMOS** complimentary metal-oxide-semiconductor

**MEMS** micro-electro-mechanical systems

**WDM** wavelength division multiplexing

**QFT** quantum field theory

# Acknowledgements

First, I would like to thank my supervisor, Dr. Lukas Chrostowski, for his inspiration, support, and for all of the opportunities he has provided. I am also thankful to my other committee members, Dr. Nicolas Jaeger and Dr. Sudip Shekhar, for their time, useful feedback, and insight.

I would like to thank all of my colleagues for their support and friendship, in particular M. Caverley, M. Guillén-Torres, H. Jayatilleka, Z. Lu, and S. Talebi Fard, for their assistance and collaboration.

I offer thanks to Ranovus Inc. for providing an internship opportunity during my studies.

I gratefully acknowledge CMC Microsystems, Huawei, and the Natural Sciences and Engineering Research Council of Canada, including the Si-EPIC program, for financial support. I would also like to thank Lumerical Solutions Inc. and Mentor Graphics Inc. for the design tools used in this work.

# Chapter 1

# Introduction

## 1.1 Current State of Silicon Photonic Switches

Silicon photonics has recently generated a great deal of interest for telecommunications applications. Due to the compatibility of silicon-on-insulator (SOI) platforms with mature complimentary metal-oxide-semiconductor (CMOS) electronics fabrication technologies, silicon photonics offers the potential for inexpensive integration with the electronics needed for their operation. Numerous types of devices have been implemented on SOI including filters [4–6], switches [7], modulators [8, 9], detectors [10–12], sensors [13, 14], and polarization splitters and/or rotators [15, 16]. Several companies have invested into silicon photonics research, including IBM, who have demonstrated monlithic integration of $8\times8$ silicon photonic switches with CMOS control [17], and Intel, who have demonstrated a 4-channel silicon photonics wavelength division multiplexing (WDM) links with integrated electronics [18]. Despite the recent interest in developing large systems, it is still important to improve performance at the device level.

Early demonstrations of thermo-optic switches on SOI required large power consumption due to the inefficiency of the phase shifters used [19]. As the number of switches in a network is increased, the power consumption of each individual switch will become more important as the waste heat produced requires increasingly complex thermal management [20].

Switches on an SOI platform can be implemented using a number of interferometric structures, including Mach Zehnder interferometers (MZIs) [19, 21, 22], Michelson interferometers [23], and micro-ring resonators [24, 25]. These types of switches typically require the use of optical phase shifters to implement the switching action. Phase shifters find fundamental applications in many silicon photonic devices including switches [26, 27], modulators [28, 29], and tunable filters [30]. Two common ways of implementing a phase shifter rely on the plasma dispersion effect [31], in which a change in the density of charge carriers affects the refractive index of silicon, and the thermo-optic effect [32], in which a temperature change affects the refractive index. Plasma dispersion-based phase shifters, while offering fast operation, often require large footprints or high operating voltages and have an optical loss modulation associated with the phase shift [31]. Thermo-optic phase shifters can achieve large phase shifts in small footprints with low operating voltages and without introducing optical loss modulation. However, they have slower response times and typically require more power for switching [33, 34].

As an alternative to interferometry-based switches, micro-electro-mechanical systems (MEMS), in which switching is achieved by electrically modulating the motion of waveguides, have been proposed as potential alternatives to interferometric switching requiring phase shifters. Both experimental and theoretical analysis of MEMS-based switches have been presented [35, 36]. MEMS-based switches offer both low switching power and high switching speed. However, they require moving parts and so are generally expected to have shorter lifetimes than devices with no moving parts [37]. MEMS-based switches using various operating principles have been demonstrated. For example, the modulation of the distance between parallel waveguides has been used to modulate the amount of evanescent coupling, and thus the total cross-coupling, in a directional coupler switch [35, 38]. Alternatively, modulation of the air gap between concatenated waveguides has been used to modulate the amount of transmission between the waveguides [39]. MEMS-based switches have been used to create $50\times50$ switch networks [40].

The focus of this thesis is on interferometry-based switches, and in particular, on the design of highly efficient thermo-optic phase shifters.

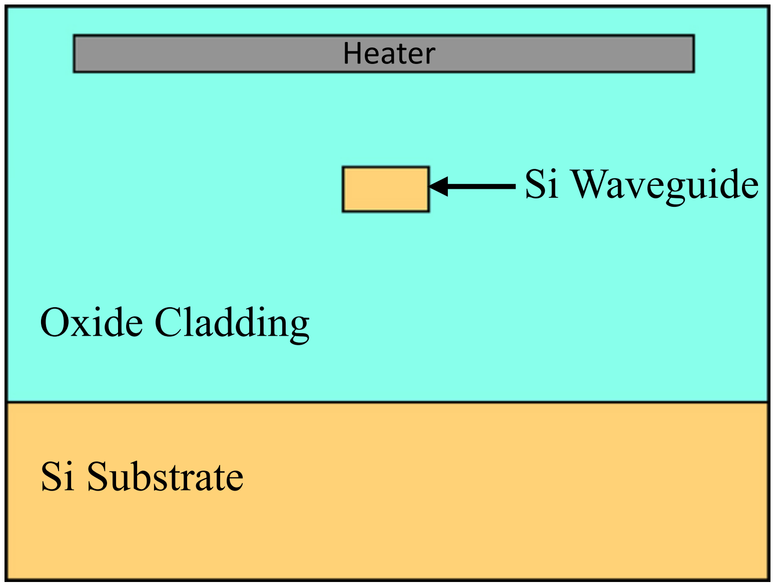


**(a)**

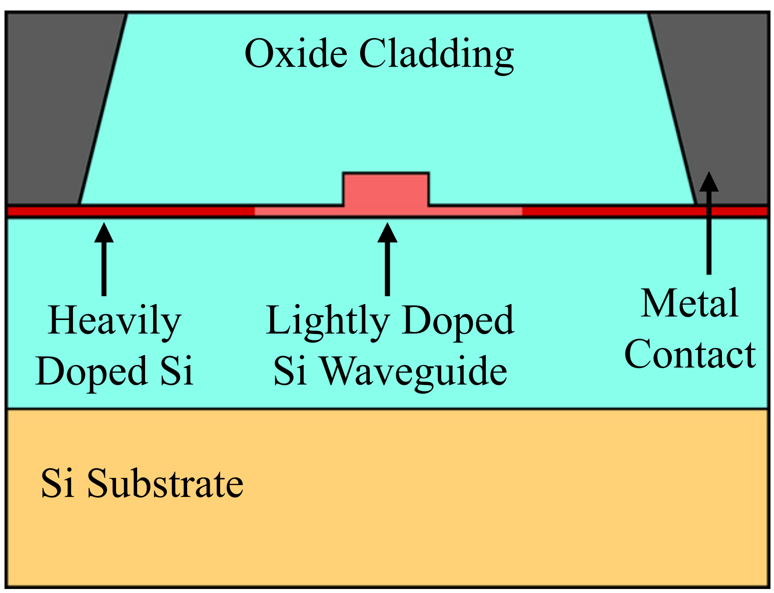


**(b)**

**Figure 1.1:** a) Cross-section of a phase shifter with a metal heater. b) Cross-section of a phase shifter with a doped silicon heater.

## 1.2 Literature Review

The heating element in thermo-optic phase shifters has been implemented in multiple ways. Figures 1.1 a) and b) show schematic cross-sections of heaters implemented using metallic heaters, and using doped silicon heaters, respectively. Most demonstrations of thermo-optic switches have utilized metallic heaters. These heaters are typically positioned several microns above a waveguide to be heated, in order to prevent absorption of light by the heater. Since the rate of heat loss to convection at the cladding surface is typically smaller than the rate of heat loss to conduction to the silicon substrate, due to the large thermal conductivity of silicon, the need for the metal heater to be kept away from the waveguide does not dramatically decrease efficiency. A drawback of using such metal heaters is that, due to fabrication limits, the heater must usually be significantly wider than the waveguides. This results in the heating of a large volume of cladding oxide that does not contribute to a phase shift. Heaters formed by doped silicon have the advantage of heating the silicon directly. However, a silicon slab is needed to make electrical contact to the doped silicon. The conduction of heat away from the waveguide along the slab region results in a degraded thermal efficiency. Additionally, the need to dope the silicon results in an increase in optical loss. Phase shifters utilizing doped heaters have been demonstrated in [41, 42].

Thermo-optic phase shifters on SOI have shown orders of magnitude reduction in switching power over the last decade [2]. This has been a result of a number of methods for increasing the efficiency of thermo-optic phase shifters being proposed. The most effective of these methods include improving thermal isolation by the removing the material surrounding the phase shifters [43–45], and folding a waveguide many times under a heater to increase the optical interaction length with the heated region [7, 46]. When folding a waveguide under a heater, the waveguide spacing between each fold is limited by the evanescent coupling of light between adjacent waveguides. When adjacent waveguides are identical, the coupling of power between them is resonant, and a complete transfer of power occurs over a characteristic coupling length [47]. The coupling length is strongly dependent on the waveguide spacing, and so the spacing must be chosen such that the power coupling over the length of the device is sufficiently small for a desired application.

This need for a sufficiently large spacing limits the achievable density of waveguide routing and, therefore, limits the number of times a waveguide can be folded under a heater and its power efficiency. In this work we propose utilizing different waveguide widths in each fold of a phase shifter to overcome this limit. The evanescent coupling between dissimilar waveguides does not achieve phase matching. Therefore, the power coupling between waveguides is not complete [48]. For a given waveguide spacing, if the mismatch between adjacent waveguide widths is sufficiently large, then the power coupling can be made negligibly small over any coupling length. Without the need to have a large spacing, the density of waveguide folding under a heating element can be increased dramatically, and the efficiency of thermal heaters can be correspondingly improved.

Prior to this work, the use of dissimilar waveguides to increase waveguide routing density in photonic circuits was proposed [3, 49], and an in depth analysis in this context has been performed [50]. More recently, dissimilar waveguide routing has also been proposed for dense mode division multiplexing, with gaps between adjacent waveguides as small as 100 nm [51]. After the submission of [, 1] Mrejen et al. demonstrated control of the coupling between two waveguides by controlling the refractive index of an intermediate dissimilar waveguide [52]. We have recently demonstrated a Michelson interferometer using dissimilar waveguide routing, showing that the technique suggested herein can be extended to other switching architectures to achieve extremely low switching power [2].

## 1.3 Objective of this Thesis

In this thesis, the use of dense dissimilar waveguide routing in folded waveguide thermo-optic phase shifters is proposed, with the objective of reducing the power consumption required for switching. The optical properties of such folded waveguide structures are modelled to assess their feasibility, to identify important considerations in their design, and to provide metrics for evaluating their performance. Thermal and mechanical models of the structure are also developed in order to optimize the structure's performance, and to provide predictions against which experimental results can be compared.

## 1.4 Overview

This thesis consists of four chapters. In this chapter, an introduction to the uses of silicon photonic switches, as well as an overview of the state of the art and current challenges in implementing these switches, with particular attention made to thermo-optic phase shifters, is presented. A review of the literature is also presented, and the objectives of this thesis are outlined. In Chapter 2, models of the optical, mechanical, and thermal properties of the phase shifters designed in this work are developed. In Chapter 3, the design of the switches that were fabricated are described in detail, and the results of experiments are presented. The experimental results are compared against those of previous works. In Chapter 4, conclusions are drawn and suggestions for future work are made.

# Chapter 2

# Theoretical Device Analysis

## 2.1 General Switch Structure

Figure 2.1 a) shows a schematic of an ideal $2 \times 2$ MZI. The MZI consists of a 50-50 beam splitter, two phase arms, and a second 50-50 beam splitter. The electric fields at the upper and lower ports of the input coupler are denoted by $E_{\mathrm{In}1}$ and $E_{\mathrm{In}2}$, respectively, while the electric fields at the output coupler are similarly denoted by $E_{\mathrm{Out}1}$ and $E_{\mathrm{Out}2}$. Figure 2.1 b) shows a schematic of the 50-50 beam splitter. The electric fields at the upper and lower ports of the input are denoted by $E_A$ and $E_B$, respectively, while the electric fields at the two output ports are denoted by $E_C$ and $E_D$. The relationship between the input and output fields of the coupler depends on the particular design of the coupler. For the adiabatic coupler used in this work, the fields are related as [53]

$$\begin{bmatrix} E_C \\ E_D \end{bmatrix} = \frac{1}{\sqrt{2}} \begin{bmatrix} 1 & 1 \\ -1 & 1 \end{bmatrix} \begin{bmatrix} E_A \\ E_B \end{bmatrix} \equiv T_{50\text{-}50} \begin{bmatrix} E_A \\ E_B \end{bmatrix}. \tag{2.1}$$

Supposing that light with unit electric field amplitude is input into the upper port of the input coupler of the MZI, the fields at the MZI output are then given by

$$\begin{bmatrix} E_{\mathrm{Out}1} \\ E_{\mathrm{Out}2} \end{bmatrix} = T_{50\text{-}50}^{-1} \begin{bmatrix} e^{i\phi_1} & 0 \\ 0 & e^{i\phi_2} \end{bmatrix} T_{50\text{-}50} \begin{bmatrix} 1 \\ 0 \end{bmatrix} \equiv T_{\mathrm{MZI}} \begin{bmatrix} 1 \\ 0 \end{bmatrix}, \tag{2.2}$$

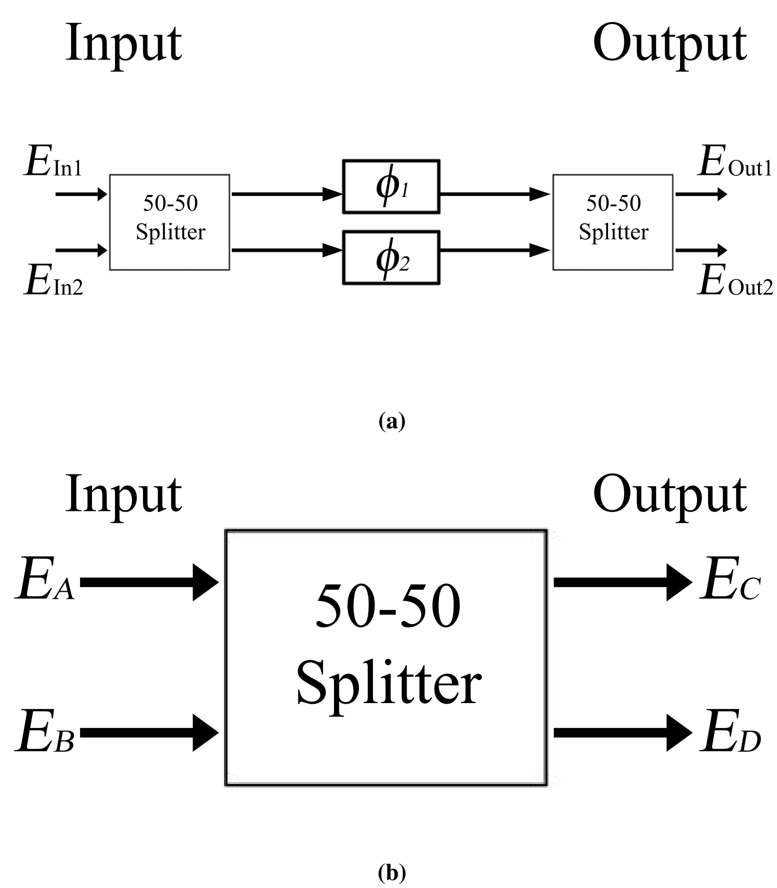


**Figure 2.1:** a) A schematic of an MZI. b) A 50-50 Splitter

where $\phi_1$ and $\phi_2$ are the phases acquired along the upper and lower arms of the MZI, respectively. The fields at the output then satisfy

$$|E_{\mathrm{Out1}}|^2 = \cos^2\left(\frac{\phi_1 - \phi_2}{2}\right) \tag{2.3}$$

and

$$|E_{\mathrm{Out2}}|^2 = \sin^2\left(\frac{\phi_1 - \phi_2}{2}\right). \tag{2.4}$$

Thus, if the phase difference between the arms can be changed from 0 to $\pi$, then the intensity at an output arm can be changed from a maximum to a minimum value, or vice versa. This effect can be used to make switches, but also provides a straightforward way to characterize the performance of a phase shifter. The following sections consist of an analysis of a particular implementation of a phase shifter.

## 2.2 Optical Modelling

In many applications a switch is, ideally, expected to simply change which direction light exits the switch without modifying any of its other properties. For example, an ideal switch should not introduce light reflection at the switch input, introduce additional loss, or introduce dispersion. In this section we introduce two models of light propagation in the folded waveguide structure that forms the interferometer arms of the switches discussed in Section 2.1. The first model, based on coupled mode theory gives an analytical expression of the transmission and dispersion of the folded waveguide structure. However, this model does not provide any intuitive explanation of the behaviour of light in the structure. The second model developed, based on a formal path integral approach provides this intuitive explanation, although it is computationally infeasible to implement in the general case. Together, the models provide both quantitative descriptions of the folded waveguide structure's optical properties and a useful way of thinking about the structure.

### 2.2.1 Coupled Mode Theory of Dissimilar Waveguides

In this section we compute the crosstalk between a pair of dissimilar waveguides. To achieve this, we define a notion of the power in a waveguide by projecting the optical field of the two-waveguide system onto the field of a single waveguide mode. We perform a change of basis from the two-waveguide eigenmode basis, in which the propagation is simple to describe, to a basis in which the power in each waveguide is simple to compute. In this basis the propagation is more complicated due to the appearance of coupling between modes.

Consider two parallel waveguides, denoted as waveguides A and B, of thickness $t$ and widths $w_\mathrm{A}$ and $w_\mathrm{B}$ separated by a gap, $g$, as shown in Fig. 2.2. The two waveguide system has transverse electric (TE) eigenmodes $|1\rangle$ and $|2\rangle$, each normalized to unit power, with propagation constants $k_1$ and $k_2$ respectively. Waveguides A and B considered in isolation have eigenmodes $|A_0\rangle$ and $|B_0\rangle$, respectively.

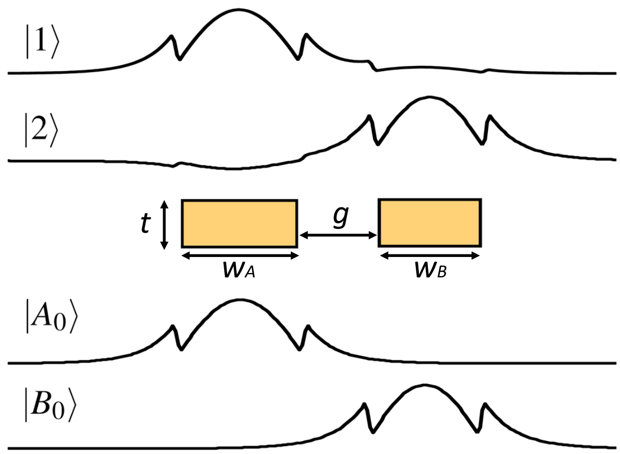


**Figure 2.2:** Dissimilar waveguide structure and horizontal electric field profile of its modes. Modes $|1\rangle$ and $|2\rangle$ are the modes of the two-waveguide structure. Modes $|A_0\rangle$ and $|B_0\rangle$ are the modes when only waveguide A or waveguide B are present, respectively. ©Optical Society of America, 2015, by permission.

With the inner product [48]:

$$\langle \psi_1 | \psi_2 \rangle = \frac{1}{4} \left[ \int \mathbf{E}_1 \times \mathbf{H}_2^* \cdot \mathrm{d}\mathbf{S} + \int \mathbf{E}_2^* \times \mathbf{H}_1 \cdot \mathrm{d}\mathbf{S} \right], \tag{2.5}$$

where $\mathbf{E}_i$ and $\mathbf{H}_i$, $i = 1,2$, are the transverse electric and magnetic field profiles of any two modes $|\psi_i\rangle$ and $\mathbf{S}$ is the plane normal to the propagation direction, we can decompose the single waveguide state $|A_0\rangle$ in terms of the two-waveguide eigenmodes:

$$|A\rangle = \langle 1|A_0\rangle\, |1\rangle + \langle 2|A_0\rangle\, |2\rangle\,. \tag{2.6}$$

The difference between $|A\rangle$ and $|A_0\rangle$ is due to not including the complete set of radiation modes in the mode decomposition. Define the power normalized state

$$|\bar{A}\rangle = \frac{|A\rangle}{\sqrt{\langle A|A\rangle}}, \tag{2.7}$$

and $|\bar{B}\rangle$ similarly. A general superposition in the $|1\rangle$, $|2\rangle$ basis is then denoted as a vector with components $a$ and $b$:

$$\mathbf{V} = \begin{bmatrix} a \\ b \end{bmatrix} = a\,|1\rangle + b\,|2\rangle\,. \tag{2.8}$$

Evolution along the propagation direction, $z$, is given by:

$$\frac{\mathrm{d}\mathbf{V}}{\mathrm{d}z} = i \begin{bmatrix} k_1 & 0 \\ 0 & k_2 \end{bmatrix} \mathbf{V} \equiv iP\mathbf{V}. \tag{2.9}$$

Performing a change to the $|\bar{A}\rangle$, $|\bar{B}\rangle$ basis with components $c$ and $d$,

$$\bar{\mathbf{V}} = \begin{bmatrix} c \\ d \end{bmatrix} = c\,|\bar{A}\rangle + d\,|\bar{B}\rangle \tag{2.10}$$

$$\mathbf{V} = \begin{bmatrix} \frac{\langle 1|A_0\rangle}{\sqrt{\langle A|A\rangle}} & \frac{\langle 1|B_0\rangle}{\sqrt{\langle B|B\rangle}} \\ \frac{\langle 2|A_0\rangle}{\sqrt{\langle A|A\rangle}} & \frac{\langle 2|B_0\rangle}{\sqrt{\langle B|B\rangle}} \end{bmatrix} \bar{\mathbf{V}} \equiv M\bar{\mathbf{V}}, \tag{2.11}$$

the new evolution follows:

$$\frac{\mathrm{d}\bar{\mathbf{V}}}{\mathrm{d}z} = iM^{-1}PM\bar{\mathbf{V}} \equiv i\bar{P}\bar{\mathbf{V}}. \tag{2.12}$$

It should be noted that since in general $M$ is not unitary the inner product is

$$\mathbf{V}^\dagger\mathbf{V} = \bar{\mathbf{V}}^\dagger M^\dagger M\bar{\mathbf{V}} \neq \bar{\mathbf{V}}^\dagger\bar{\mathbf{V}}, \tag{2.13}$$

where † indicates the conjugate transpose operation, so the sum of the squares of the norms of the components of $\bar{\mathbf{V}}$ is not in general a conserved quantity. Nevertheless, we will identify the squares of the norms of the components of $\bar{\mathbf{V}}$ with the informal notion of the power contained in each waveguide. More precisely, the square of the norm of the first component of $\bar{\mathbf{V}}$ is the power that would be transmitted in to waveguide A if waveguide B were abruptly terminated and the squared norm of the second component has a similar interpretation.

If we consider a situation where at $z = 0$ the waveguide system is excited in the state $|\bar{A}\rangle$, then one can consider the power coupled to waveguide B over some length $L$ as the squared norm of the amplitude of $|\bar{B}\rangle$ at $z = L$. In the special case where waveguides A and B are identical, the power is transferred completely from waveguide A to waveguide B over a characteristic length, $L_c = \pi/(k_1 - k_2)$, depending on the dimensions of the waveguides and their separation [48]. Thus, if one wishes to limit the crosstalk between the waveguides over their length, then the separation between the waveguides must be made large enough such that $L_c >> L$.

If the two waveguides are not identical, then the power is still periodically coupled between the waveguides, but the transfer of power is incomplete [48]. The maximum crosstalk, CT, can then be computed as the maximum value of the squared norm of the second component of $\bar{\mathbf{V}}$ in the solution to Eq. (2.12):

$$\bar{\mathbf{V}}(z) = M^{-1} e^{iPz} M\, \bar{\mathbf{V}}(0) = M^{-1} e^{iPz} M \begin{bmatrix} 1 \\ 0 \end{bmatrix} \tag{2.14}$$

$$\begin{aligned} \mathrm{CT} &= \max_z \left( |\,[0\;\;1]\, \bar{\mathbf{V}}(z)|^2 \right) = \max_z \left( \left| [0\;\;1]\, M^{-1} e^{iPz} M \begin{bmatrix} 1 \\ 0 \end{bmatrix} \right|^2 \right) \\ &= 4 \cdot \frac{\langle B|B\rangle}{\langle A|A\rangle} \cdot \frac{|\,\langle 1|A_0\rangle \langle 2|A_0\rangle\,|^2}{|\,\langle 1|A_0\rangle \langle 2|B_0\rangle - \langle 1|B_0\rangle \langle 2|A_0\rangle\,|^2} \end{aligned} \tag{2.15}$$

Figure 2.3 shows the computed maximum crosstalk for waveguides with a fixed center to center separation of 1 $\mu$m and thickness 220 nm as the widths of the waveguides are varied for a wavelength of 1550 nm [3]. The modes and propagation constants were computed using a numerical mode solver. It can be seen that by making the waveguide widths sufficiently different the crosstalk can be limited for small separations regardless of the length of the coupler. The asymmetry of the crosstalk under interchange of waveguide A and B is due the difference between first exciting state $|A\rangle$, then later measuring state $|B\rangle$, and first exciting state $|B\rangle$, then later measuring state $|A\rangle$. This difference is due to the non-orthogonality of $|A\rangle$ and $|B\rangle$ for dissimilar waveguides.

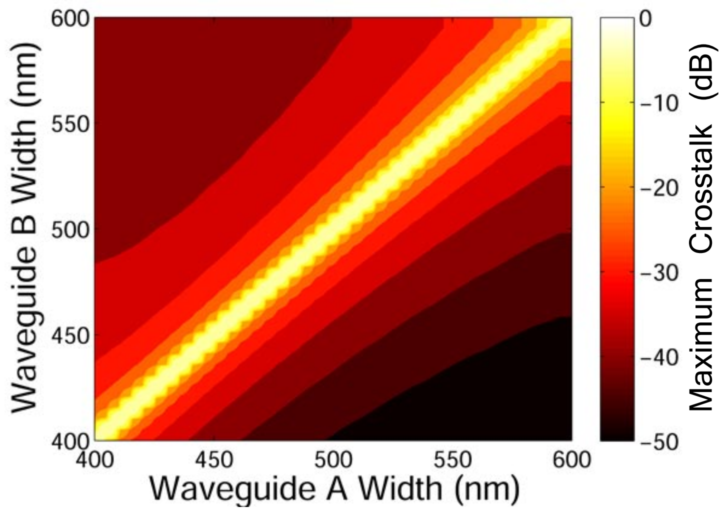


**Figure 2.3:** Maximum crosstalk between 220 nm thick waveguides with 1 $\mu$m pitch. ©Optical Society of America, 2015, by permission.

### 2.2.2 Folded Waveguide Structures

#### A Coupled Mode Approach

Figure 2.4 shows a schematic of the folded waveguide structure consisting of a waveguide folded $N$ times, with widths $w_m$, $m = 1, 2, ..N$. Light is injected into waveguide 1 and the transmitted light is measured at waveguide $N$. We consider only an odd number of waveguides so that the input and transmitted light are travelling in the same direction. To model the propagation, we utilize a tight-binding coupled mode model where we consider coupling only between nearest neighbour waveguides. The propagation is described by the differential equations:

$$\frac{\mathrm{d}\bar{V}_m^+}{\mathrm{d}z} = a_m \bar{V}_m^+ + b_m \bar{V}_{m-1}^+ + c_m \bar{V}_{m+1}^+ \tag{2.16}$$

$$\frac{\mathrm{d}\bar{V}_m^-}{\mathrm{d}z} = -a_m \bar{V}_m^- - b_m \bar{V}_{m-1}^- - c_m \bar{V}_{m+1}^-, \tag{2.17}$$

where $\bar{V}_m^+$ and $\bar{V}_m^-$, $m = 1, 2, ...N$, are the amplitudes of the modes in waveguide $m$ travelling in the positive and negative $z$ directions, respectively. Here $a_m$, $b_m$,

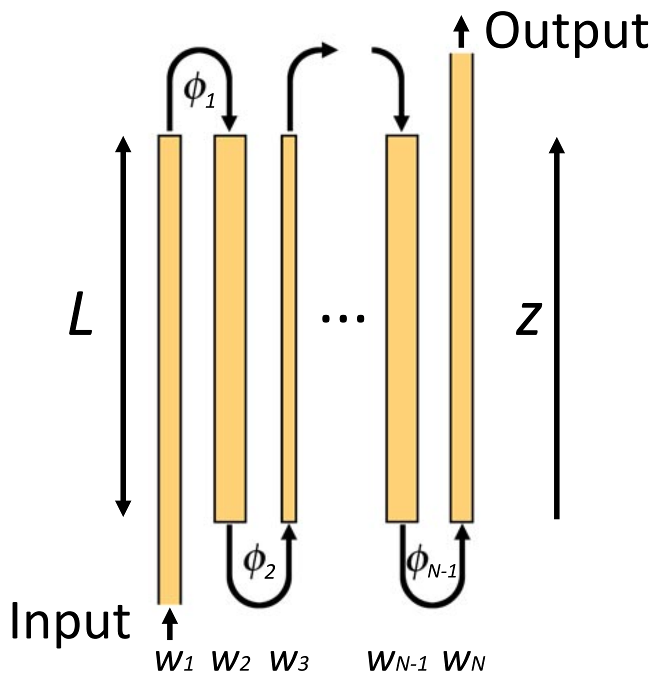


**Figure 2.4:** Schematic diagram of folded waveguide structure. ©Optical Society of America, 2015, by permission.

and $c_m$ are the pairwise self and cross coupling coefficients computed as described in equation (2.12). Specifically, $a_m$ are the self coupling coefficients found as the diagonal elements of $i\bar{P}$, and $b_m$ and $c_m$ are the cross-coupling coefficients found as the off-diagonal elements of $i\bar{P}$. Further, the system adheres to the boundary conditions:

$$\bar{V}_0^+(0) = 1 \tag{2.18}$$

$$\bar{V}_N^-(L) = 0 \tag{2.19}$$

$$\left.\begin{aligned} \bar{V}_m^-(L) &= \bar{V}_{i-1}^+(L)e^{i\phi_{m-1}} \\ \bar{V}_m^+(L) &= \bar{V}_{m-1}^-(L)e^{-i\phi_{m-1}} \end{aligned}\right\} \text{ for } m \text{ even} \tag{2.20}$$

$$\left.\begin{aligned} \bar{V}_m^-(0) &= \bar{V}_{m-1}^+(0)e^{i\phi_{m-1}} \\ \bar{V}_m^+(0) &= \bar{V}_{m-1}^-(0)e^{-i\phi_{m-1}} \end{aligned}\right\} \text{ for } m \text{ odd}, m > 1, \tag{2.21}$$

where $\phi_m$ is the phase associated with the bend connecting waveguide $m$ with waveguide $m+1$. To solve the boundary value problem described by equations 2.16 and 2.17, subject to the boundary conditions of equations 2.18-2.21, we construct vectors $\bar{\mathbf{V}}^+$ and $\bar{\mathbf{V}}^-$ with components $\bar{V}_m^+$ and $\bar{V}_m^-$, respectively. Equations 2.16 and 2.17 can then be written in matrix form as

$$\frac{\mathrm{d}\bar{\mathbf{V}}^+}{\mathrm{d}z} = S\bar{\mathbf{V}}^+ \tag{2.22}$$

$$\frac{\mathrm{d}\bar{\mathbf{V}}^-}{\mathrm{d}z} = -S\bar{\mathbf{V}}^-, \tag{2.23}$$

where the propagation matrix, $S$, is

$$S = \begin{bmatrix} a_1 & c_1 & 0 & 0 & \ldots & 0 \\ b_2 & a_2 & c_2 & 0 & \ldots & 0 \\ 0 & b_3 & a_3 & c_3 & \ldots & 0 \\ . & . & & & & \\ . & & . & & & \\ . & & & . & & \\ 0 & 0 & \ldots & 0 & b_N & a_N \end{bmatrix}. \tag{2.24}$$

Equations 2.16 and 2.17 have general solutions

$$\bar{\mathbf{V}}^+(z) = e^{Sz}\bar{\mathbf{V}}^+(0) \tag{2.25}$$

$$\bar{\mathbf{V}}^-(z) = e^{-Sz}\bar{\mathbf{V}}^-(0). \tag{2.26}$$

Evaluating these equations at $z = 0$ and $z = L$, the boundary conditions given by equations 2.18-2.21 constitute a set of $2N$ coupled linear equations for the initial values of the components of $\bar{\mathbf{V}}^+(0)$ and $\bar{\mathbf{V}}^-(0)$, which are readily solved by a matrix inversion. The field reflection and transmission are then $\bar{V}_1^-(0)$ and $\bar{V}_N^+(L)$, respectively.

The system of equations (2.16, 2.17) was numerically solved for $N = 9$, $L = 90$ $\mu$m, and identical waveguides with a thickness of 220 nm, a width of 500 nm, and gaps between the waveguides of $g$ = 500 nm, 750 nm, and 1 $\mu$m. Additionally, the system of equations was solved for a system consisting of alternating waveguides with 500 nm and 600 nm widths separated by a gap of 500 nm for $N = 9$, and $L = 90\ \mu$m. The phases $\phi_m$ from the bends were all set to zero for simplicity. The results as a function of wavelength are presented in Figure 2.5 a). It is clear that in the case of identical waveguides there is already significant ripple in the spectrum for a gap of 750 nm, and that a stop band appears for a gap of 500 nm. With the dissimilar waveguides, however, the ripple in the spectrum for a gap of 500 nm is less than that for the identical waveguides at a gap of 1 $\mu$m. The shape of the spectrum depends strongly on the phases $\phi_j$, however, the degree of ripple in the spectrum does not. This would generally hold true for more realistic, wavelength dependent, phases associated with the bends as well. The degree of ripple was characterized by computing the minimum transmission of the folded waveguide structure as the gap between the waveguides was varied. The results are presented in Fig. 2.5 b). It can be seen that for identical waveguides, the ripple in the spectrum causes the transmission to rapidly fall off for waveguide separations less than 1 $\mu$m. On the other hand, the reduction in crosstalk between the dissimilar waveguides effectively keeps the spectrum from developing significant ripple until the waveguide separation is less than 500 nm.

Figure 2.6 shows the calculated intensity of the forward and backward travelling light along the length of a device, following the waveguides without cross-coupling, for a folded waveguide structure with 9 identical waveguides. The waveguides have a width of 500 nm, and a gap between them of 500 nm. The transmission of this structure is shown in Figure 2.5 a), which shows that the transmission is high for some wavelengths, which will be called the On state, and low for some wavelengths, which will be called the Off state. In Figure 2.6, it can be seen that in the Off state the amount of forward travelling light decays quickly along the length of the structure as the light cross-couples into a backward travelling mode. In contrast, in the On state the behaviour is much more interesting. First, perhaps contrary to expectation, the backward travelling mode has significant intensity over most of the structure, only decaying to zero in the first and last waveguides. Secondly, there is a resonant buildup of intensity in the forward travelling mode over the entire structure, excepting the input and output. Supposing that the resonant buildup of intensity relies on a ring resonator-like closed path for light in the struc-

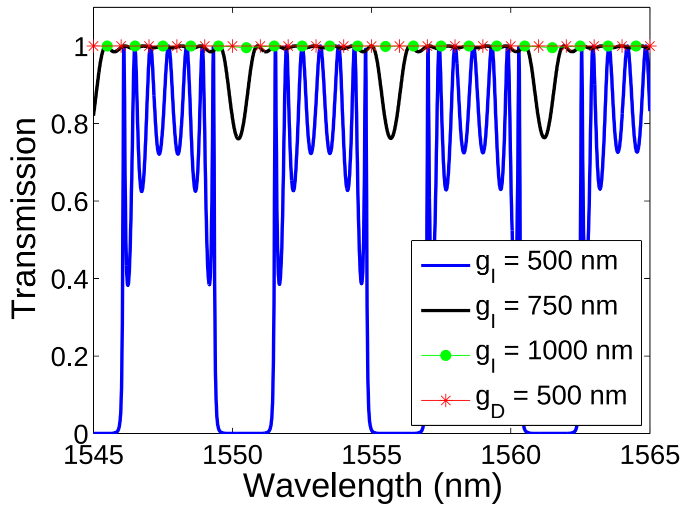


**(a)**

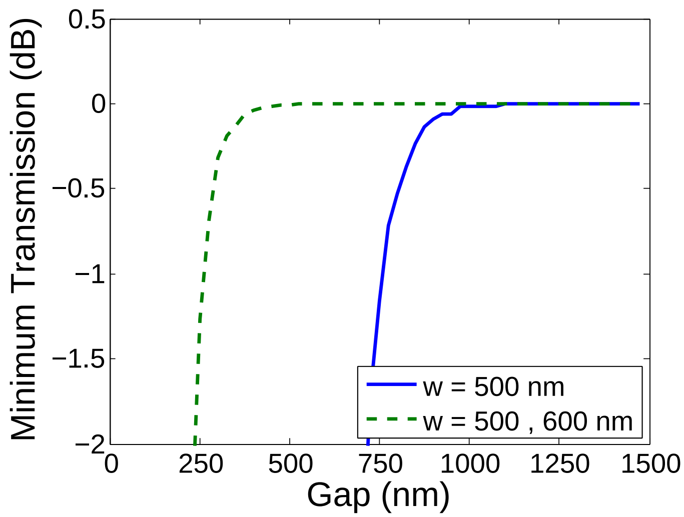


**(b)**

**Figure 2.5:** a) Calculated spectra of the folded waveguide structure for 9 identical waveguides with gaps $g_I = 500$ nm, 750 nm, and 1000 nm, and alternating dissimilar waveguides with widths of 500 nm and 600 nm with gap $g_D = 500$ nm, b) Minimum transmission of the folded waveguide structure for similar (solid) and dissimilar (dashed) waveguides. ©Optical Society of America, 2015, by permission.

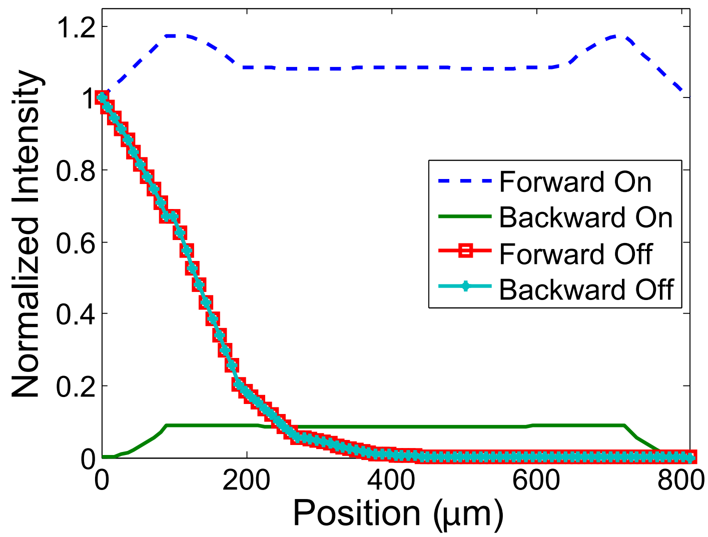


**Figure 2.6:** Intensity of forward and backward travelling modes as a function of position along the folded waveguide structure, measured as the distance along the path with no cross-coupling. The 9 waveguides are all of 500 nm width, 90 $\mu$m length, and the gap is 500 nm. The On state is at 1553.16 nm and the Off state is at 1556 nm.

ture, like in an example that is discussed below, this observation can help explain the observation about the backward travelling mode. This is because, as it is simple to convince oneself of, any closed path in the structure necessarily requires some portion of the path laying in a backward travelling mode. These results show that a structure as simple as a folded waveguide can exhibit rich and non-obvious behaviour.

A simple argument shows that the neglect of next-to-nearest neighbour coupling, and more generally any coupling across an even number of waveguides, does not effect the degree of ripple in the through spectrum for lossless waveguides. To see this, consider a hypothetical system where nearest-neighbour coupling is negligible but coupling to next-to-nearest neighbour waveguides is not, which can be approximately implemented with waveguides of alternating widths. In this case, due to the geometry of the folded waveguides, no amount of coupling can result in light propagating backwards. Thus, there can be no reflected signal. Due to conservation of energy, one can conclude that at all wavelengths the transmission must be unity. In the case where nearest-neighbour coupling is also present, the effect of next-to-nearest neighbour coupling would be to change the wavelengths where constructive and destructive interference occur, but not the degree of interference.

**A toy model of next-to-nearest waveguide coupling in lossy waveguides**

Here, a toy model of next-to-nearest neighbour coupling in lossy waveguides is presented to explore its effects.

Consider a folded waveguide structure with $N = 3$, where the first and third waveguides are identical and the second waveguide is dissimilar from the other two. Coupling can then be assumed to occur only between the first and third waveguides. Figure 2.7 a) shows a schematic of the structure. Let the phase acquired along each of the two identical waveguides be $\phi_C$, and the phase acquired along the bends and the intermediate wavguide be $\phi_R$. Furthermore, assume that the intermediate waveguide is lossy, with a forward field amplitude transmission $a$. Lastly, let the field through and cross-coupling coefficients of the coupler formed by the identical waveguides be $t$ and $\kappa$, respectively. The field at the output, $E_o$, for unit input can then be written as

$$E_o = i\kappa e^{i\phi_C} + t^2 a e^{i(2\phi_C+\phi_R)} \sum_{j=0}^{\infty} (i\kappa a e^{i(\phi_C+\phi_R)})^j, \tag{2.27}$$

where first term represents the light that immediately crosses to the output along the blue arrow in Figure 2.7 a), and the $j^{\text{th}}$ term in the sum represents the light that crosses through the red arrow in Figure 2.7 a) $j$ times. Summing the geometric series and simplifying using coupler power conservation, $\kappa^2 + t^2 = 1$, gives

$$E_o = e^{i\phi_C} \frac{i\kappa + a e^{i(\phi_C+\phi_R)}}{1 - i\kappa a e^{i(\phi_C+\phi_R)}}. \tag{2.28}$$

This transmission function is of the same form as a that of a first order racetrack resonator with the through coupling and cross-coupling coefficients interchanged [54]. This could also have been seen by identifying the schematic in Figure 2.7 a) with the schematic of such a racetrack resonator in Figure 2.7 b), where equivalent

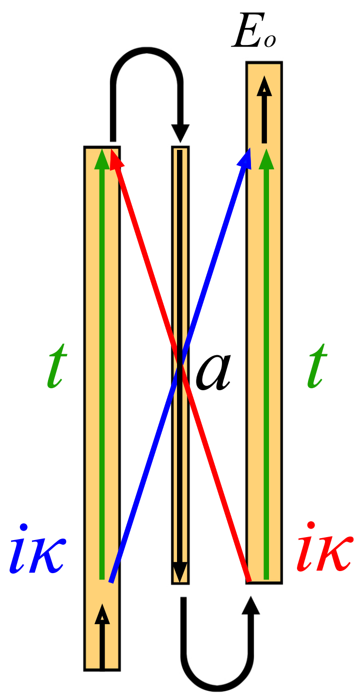


**(a)**

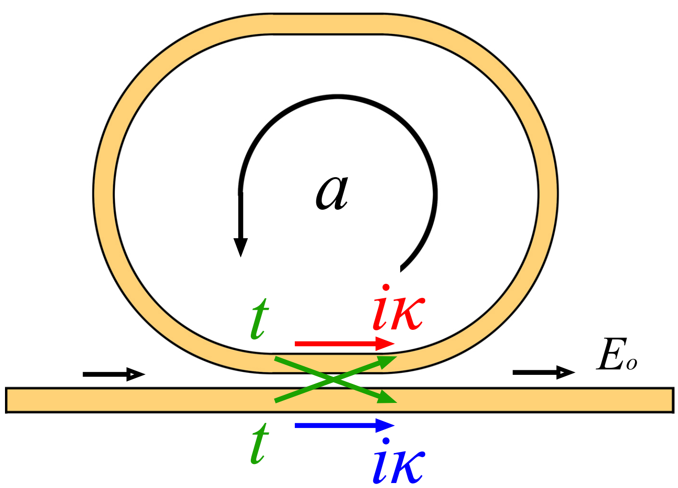


**(b)**

**Figure 2.7:** a) Folded waveguide structure with next-to-nearest neighbour coupling. b) An equivalent racetrack resonator.

paths in each device are coloured the same to help see the equivalence.

From equation 2.28, one can see that if $\kappa \approx a$, then at the resonance condition, $\phi_C + \phi_R = 3\pi/2 + 2m\pi$ for integer $m$, the transmission can be expected to drop to near zero, in stark contrast to the prediction above for the lossless case. Thus, if one wants to prevent significant ripple in the through spectrum due to resonant next-to-nearest neighbour coupling, then the coupling coefficient must be made to be much smaller than $a$. Since for reasonably short and low loss waveguides $a \approx 1$, this is not a stringent requirement.

### A Path Integral Approach

Path integral formulations of physical theories are often used in the context of quantum theory. Although non-relativistic quantum mechanics can be formulated in terms of path integrals [55, 56], most elementary presentations do not take this approach [57, 58]. On the other hand, in quantum field theory (QFT) the path integral approach is ubiquitous, and is a convenient starting point for perturbation theory [59–61]. The path integral approach, remarkably, has even been applied to the classical mechanics of particles [62], and has shown a deep relationship between quantum mechanics and statistical mechanics [63]. Feynman diagrams, introduced as a shorthand for writing down transition amplitudes in perturbative QFT as developed through the path integral approach [64], have become the basis for popular intuitive descriptions of quantum mechanical phenomenon. For example, Figure 2.8 shows a Feynman diagram for electron-electron scattering, which gives rise to the popular description of the Coulomb force as being the result of the exchange of virtual photons. In this section, it is the usefulness of the path integral approach for providing intuition that will be exploited, with ray-like paths through the folded waveguide structure playing a role analogous to that of Feynman diagrams in QFT.

Here we develop a formal path integral model of the folded waveguide structure which, while not computationally feasible to implement, provides a useful heuristic for thinking about how light propagates in the structure. Again, for simplicity we consider only nearest neighbour coupling.

Consider breaking the folded waveguide structure with $N$ identical waveguides into $M$ equal length subsections, as shown in Figure 2.9, where in propagating

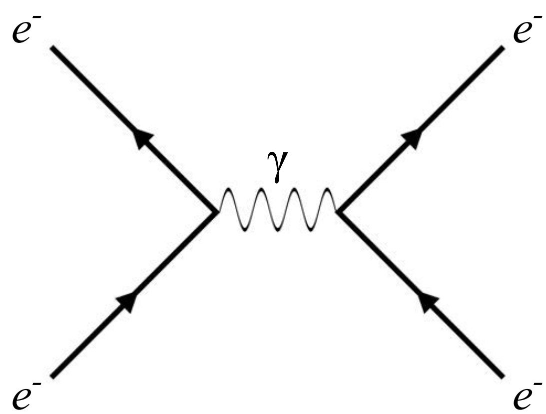


**Figure 2.8:** A Feynman diagram representing one term in an infinite sum describing electron-electron scattering through the electromagnetic field. The electrons, $e^-$, interact via the exchange of a virtual photon, $\gamma$.

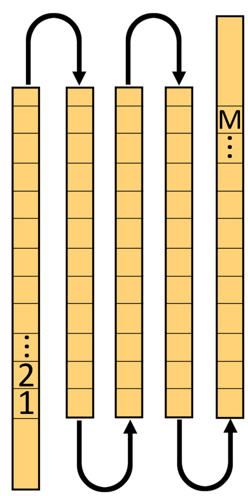


**Figure 2.9:** Folded waveguide structure divided into $M$ subsections.

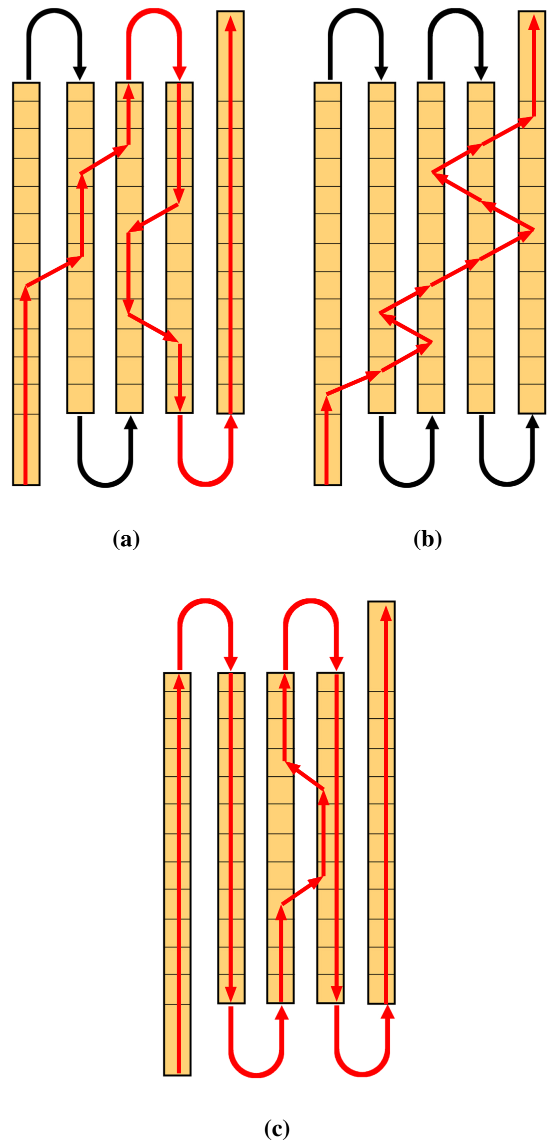


**Figure 2.10:** a) An example of a typical path through the structure, b) a path that has a large contribution for high coupling, and c) a path that has a large contribution for low coupling.

across each section the light acquires a phase, $\phi(M)$, has a field transmission coefficient, $t(M)$, and field cross-coupling coefficient, $\kappa(M)$, to the same waveguide and to each of its adjacent waveguides, respectively. One can imagine inputting light into the structure, after which it can take many paths to get to the output, some of which are illustrated for the case $N = 5$ in Figure 2.10. Since the only paths that end at the output waveguide are those that cross-couple an even number of times, these are the only paths that need to be considered. The field at the output, $E_o$, for a unit input field, can be expressed as a weighted sum over all paths,

$$E_o = t^M e^{iM\phi} + (i^2)\kappa^2 \sum_{s\in\mathbb{P}(M,2)} t^{\eta(s)} e^{i(\eta(s)+2)\phi} + (i^4)\kappa^4 \sum_{s\in\mathbb{P}(M,4)} t^{\eta(s)} e^{i(\eta(s)+4)\phi} + \dots \tag{2.29}$$

$$E_o = \sum_{l=0}^{\infty} \sum_{s\in\mathbb{P}(M,2l)} \left[(-\kappa^2 e^{2i\phi})^l t^{\eta(s)} e^{i\eta(s)\phi}\right], \tag{2.30}$$

where $\mathbb{P}(M,2l)$ is the set of paths through the folded structure discretized into $M$ segments with $l$ pairs of cross-couplings, and $\eta(s)$ is the number of segments that the light is transmitted through while propagating through the path $s$. Formally taking the limit as $M$ tends to infinity would give the true transmission of the structure, and the two sums in equation 2.30 would become an integral over all paths. The reflected field can be expressed in a similar manner as a sum over all paths with an odd number of cross-couplings. As an illuminating example, the path integral approach for a simple directional coupler is derived in Appendix A and is shown to give the correct result.

Analysing equation 2.30 in full generality is unlikely to provide any more insight into the problem than the computationally simple coupled mode model discussed above. In the limiting cases of high and low coupling, however, a picture of which paths are important can be gleaned.

For the case of high coupling, that is when $\kappa$ is 'large' and $t$ is 'small', the most important consideration that determines the strength of the contribution of a path is the number of segments through which the light is transmitted, since the $t^{\eta(s)}$ term exponentially damps the contribution of paths as this number is increased. For a fixed $l$, this means that paths are exponentially damped with increasing path length. From this, one can conclude that the most important terms in the sum will

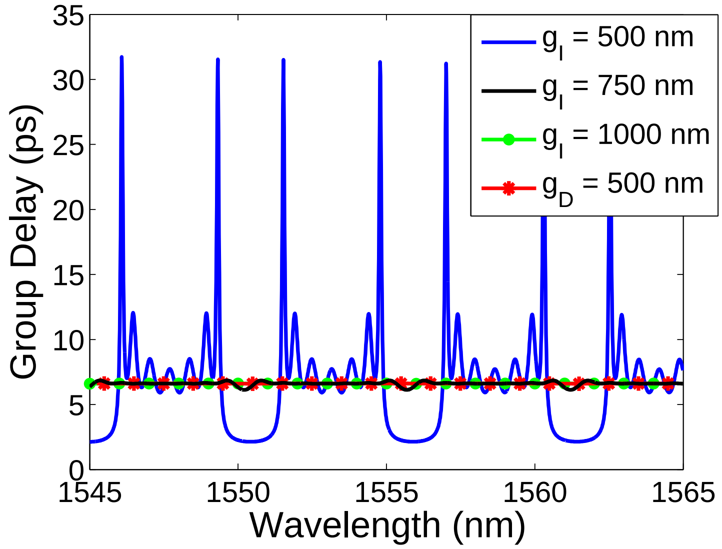


**Figure 2.11:** Calculated group delay of the folded waveguide structure for 9 identical waveguides with gaps $g_I = 500$ nm, 750 nm, and 1000 nm, and alternating dissimilar waveguides with widths of 500 nm and 600 nm with gap $g_D = 500$ nm.

be those for which coupling occurs at almost every segment, like that shown in Figure 2.10 b). In the case of low coupling, that is when $\kappa$ is 'small' and $t$ is 'large', then the contributions of paths are exponentially damped by the number of cross-couplings. Thus, to an approximation the sum over $l$ can be truncated after the first few terms. An example of a significant path for low coupling is shown in Figure 2.10 c). Of course, as $M$ goes to infinity and the segment length approaches zero the coupling coefficient must approach 0 and the transmission coefficient must approach 1. 'Small' and 'large' coupling coefficients then refer to the rate at which these coefficients change with increasing $M$.

Figure 2.11 shows the group delay, $\frac{d\phi}{d\omega}$, where $\phi$ is the phase at the output of the structure and $\omega$ is the optical angular frequency, for the structures whose transmission were calculated in Figure 2.5. For low coupling one can see that the group delay is constant, which can be interpreted as the light following the path with no cross coupling and thus having a constant propagation time through the structure given by $t = NLn/c$, where $n$ is the average refractive index and $c$ is the speed of light in vacuum. Here we have neglected the wavelength dependence of $n$ for simplicity. For high coupling, however, it can be seen that there are some wavelengths for which the group delay is less than the low coupling group delay, and some wavelengths for which the group delay is larger than that for the low coupling case. This can be interpreted by there being certain wavelengths where the light takes paths like those in 2.10 b) that are shorter than the low coupling path, and wavelengths where light takes paths containing closed loops, like those discussed in the toy model of a 3 waveguide system discussed above, that make the path longer than the low coupling path, respectively.

### The Geometrical Limit

If we consider paths that are close to each other, that is paths that are related by a small deformation, and have the same amplitude in the sum, that is have the same number of cross-couplings and transmissions, then one can discuss the geometrical optics limit of the structure. An example of a set of paths that are close together is shown in Figure 2.12, for which the deformation is parameterized by a small distance, $\delta$. If for small $\delta$ the phase acquired along each of these paths, relative to the path with $\delta = 0$, is proportional to $k\delta$ then for $kL >> 2\pi$ the sum over these paths for all $\delta$ will be an infinite sum of complex numbers with the same amplitude and phase uniformly distributed over $[0, 2\pi]$, and will sum to zero. That is to say that any path with this property can be ignored in the sum. Thus, the only paths that contribute to the sum are those for which the phase acquired is stationary with respect to small deformations in the path. This is a precise statement of Fermat's principle [65], which more loosely says that a ray of light will follow the path of shortest optical length. Applied to this structure, we can then express the wave optics solution, 2.30, as stating that the light follows all geometrically allowed paths and interferes at the structure output.

A closer look at the propagation in the structure reveals that, since transmission and cross-coupling commute (*ie.* $t\kappa = \kappa t$), the phase is stationary to small deformations for all paths. Thus, every path is geometrically allowed and Fermat's principle does not offer any simplification to equation 2.30. From this observa-

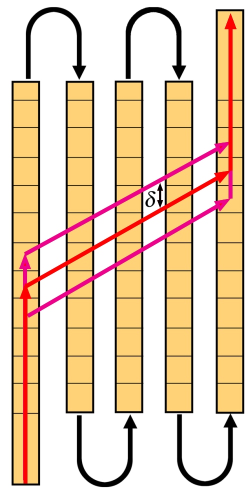


**Figure 2.12:** A set of paths that are related by a small deformation described by the parameter $\delta$.

tion we can conclude that, for non-zero coupling, propagation through the folded waveguide structure is intrinsically wave-like and its transmission cannot be well described in the language of ray optics. That is, there is no meaningful way to describe any one path that light follows through the structure. Although describing these types of devices in terms of the paths that light takes is conceptually helpful, one should be careful to not take explanations using this type of language too seriously.

The ability to discuss the propagation of light in waveguides in terms of path integrals, a technique most often encountered in quantum mechanics, is not a coincidence. The correspondence between the two types of systems is made clear by noting that equation 2.9 is of the form of the Schrödinger equation when position is interchanged with time, and the momentum operator, $P$, is interchanged with the Hamiltonian operator, $H$, in natural units ($\hbar = 1$) [57]. Due to this correspondence, a number of authors have made analogies between light propagation in $N$ coupled waveguides to the time evolution of a particle in a system with $N$ energy eigenstates [52, 66, 67]. Under this analogy, what is the quantum system corresponding to the folded waveguide structure? In the folded waveguide structure the light propagates in both the forward and backward directions. The most straightforward way to map this to a quantum system is to consider two particles in $N$ level atoms, where one of the particles is evolving backwards in time. The boundary conditions imposed on the waveguides, equations 2.18-2.21, would then represent conditions relating the state of both particles at some intitial and final times. Clearly, this is not a physically relevant system. An alternative way to map from the waveguide picture to the quantum mechanical picture is to suppose that there are two particles, both evolving forward in time, in $N$ level atoms where one of the particles has negative energy states (*ie.* is bound) and the other particle has positive energy states (*ie.* is free), where the energy eigenvalues of both systems have the same magnitude. Like in the previous example, the boundary conditions do not have an obvious physical implementation. Thus, it does not seem likely that the analogy to quantum mechanics will prove to be insightful in this case.

## 2.3 Mechanical Model

The underetching of the silicon substrate to form a suspended structure raises concerns for the mechanical stability of the phase shifter arms. During processing using liquid reactants (*eg.,* etching, cleaning, etc.) large surface tension forces can arise that may put damaging stresses on the suspended structure, or lead to stiction between the suspended structure and nearby surfaces [37]. Further, in practical applications the structure may be subject to vibrations or large accelerations. Vibrations in particular could cause time-varying stress-induced refractive index changes [68] in the waveguides that could lead to increased noise in data switching applications. In this section we investigate a simple model of the structure where the stresses induced by a uniform acceleration are calculated. While this model does not explore all types of possible mechanical modes of failure or noise generation, it gives an indication that with appropriate design these issues can likely be overcome.

Here we consider the suspended glass structures shown in Figures 2.13 a) and b). The suspended structures have a length, $L$, a 12 $\mu$m width, and thickness of 6 $\mu$m. The structure is fixed at both ends. A finite element mechanical simulation was performed assuming that the structure was undergoing a uniform acceleration,

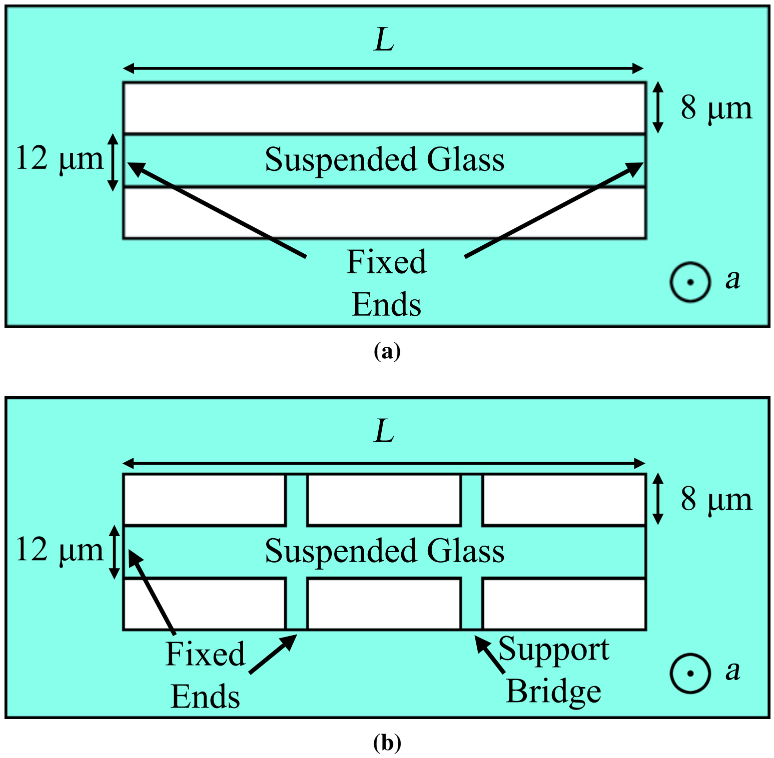


**Figure 2.13:** Top-down view of suspended glass structure a) without support bridges, and b) with two pairs of support bridges undergoing an acceleration, $a$, oriented out of the page.

$a$, in the direction normal to the chip surface. The acceleration was modelled by a uniform pressure, $P = ma/A$, distributed over the upper surface of the structure, where $m$ is the mass of the suspended glass, and $A = L \times 12$ $\mu$m is the area of the upper surface. We also considered structures where glass support bridges with a 6 $\mu$m width, 8 $\mu$m length, and fixed ends are used to support the structure along its length. The support bridges are assumed to be equally spaced along the length of the structure.

Figures 2.14 a) and 2.14 b) show the calculated von Mises stress distributions for a structure with $L = 90$ $\mu$m and $a = g$ with no support bridges, where $g = 9.8$ ms$^{-2}$ is the local acceleration due to gravity, and a structure with $L = 290$ $\mu$m and two pairs of support bridges for the same acceleration, respec-

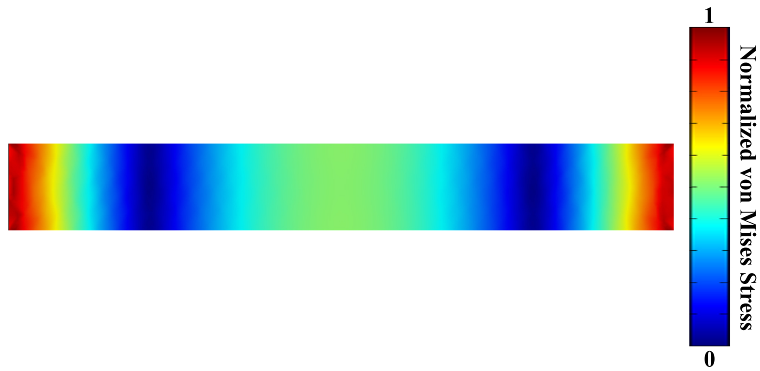


**(a)**

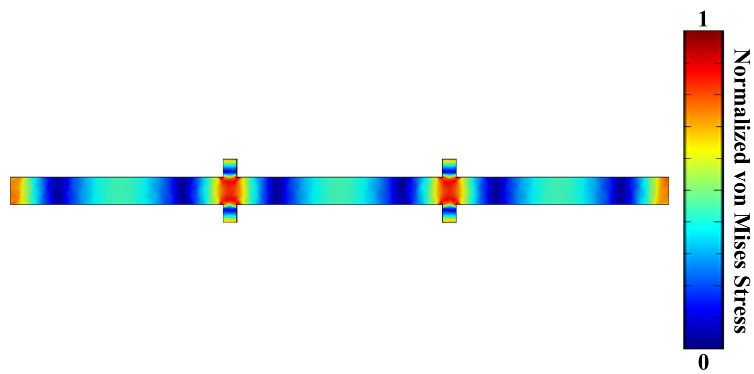


**(b)**

**Figure 2.14:** Stress distribution in a suspended heater structure under uniform $1g$ acceleration along the direction normal to the chip for a) a 90 $\mu$m long structure with no support bridges, and b) a 290 $\mu$m long structure with two pairs of support bridges.

tively.

The maximum von Mises stress was calculated for the suspended structures described above as their length was varied, and the results are shown in Figure 2.15 for an acceleration of $1g$. It is clear that adding more support bridges reduces the maximum stress, and thus will allow for a more robust structure. However, as will be shown in Section 2.4, this comes at the cost reduced thermal isolation, and thus a decrease in device efficiency. The simulations suggest that even for a 300 $\mu$m long device with no bridges, assuming even a modest yield strength of

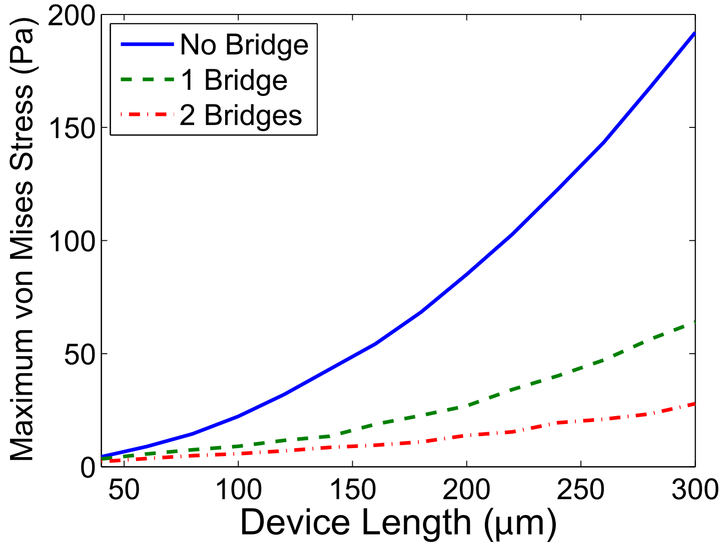


**Figure 2.15:** Maximum von Mises stress in suspended structure.

20 MPa for glass [69], the structure could withstand an acceleration of $10^5 g$ before failing, while having a maximum displacement due to deformation of only 300 nm. This strongly suggests that for reasonably sized devices structural stability will not pose an issue.

## 2.4 Thermal Model

The phase shift in thermally actuated switches is achieved through the thermo-optic effect, which is the phenomenon in which the refractive index of a material is dependent on the temperature, $T$, of the material. The thermo-optic coefficient of silicon is sufficiently large that small temperature changes can be used to cause large phase shifts over relatively small lengths [43]. In order to maximize the thermo-optic phase shift in a device for a given power it is important to consider the thermal properties of a design. Specifically, to maximize the thermo-optic phase shift in a device one must minimize the rate of heat transfer from the device to its surroundings and ensure that the heated region is localized to the region in which the light is propagating. This latter concern is to ensure that power is not wasted heating a region that does not contribute to a phase shift. Since in some applications switching times may be important in addition to the phase shifter efficiency, the effect of the methods used to optimize efficiency on respone times should also be predicted.

In this section, the results of finite element simulations of suspended structures on SOI are presented. The dependence of the thermal properties on the geometry of the structure are described, and the performance of switches utilizing a suspended structure are predicted. Figures of merit for a device's tradeoff between switching power and response time are also proposed.

The structure that was simulated consists of a glass structure of length, $L$, width, $w$, and 6 $\mu$m thickness containing $N$ silicon waveguides and a metal heater of 10 $\mu$m width inside it. The glass structure is fixed at its ends, where it is in thermal contact with the silicon substrate. The structure may also be supported along its length from below by the silicon substrate, or underetched to remove the substrate and become suspended. Further, the glass structure may have pairs of support bridges of 8 $\mu$m length, 6 $\mu$m width, and 6 $\mu$m thickness, like those considered in Section 2.3. The heater supplies a power of $P = 1$ mW uniformly over its volume. The bottom of the substrate and the edges of the chip are assumed to be at 20 °C, and all other surfaces are assumed to lose heat by convection. For simplicity, the convection coefficient was approximated as that due to free convection at the surface of a 1 cm$\times$1 cm horizontal plate. That is, the convection coefficient at each surface is approximated as being the same as that which would occur over the surface of an unpatterned chip. The effect of thermal radiation was neglected because the temperature changes needed for a $\pi$ phase shift were small due to the long lengths of the waveguides used. The thickness of the substrate and distance to the chip edge in the simulation were determined through convergence testing. The devices that were fabricated, as described in Table 3.1, will be frequently used here as examples.

The power required for switching is determined as the power that results in a phase change of $\pi$ over the length of the folded waveguides. Specifically,

$$\pi = \frac{2\pi}{\lambda}\frac{\mathrm{d}n_{\mathrm{eff}}}{\mathrm{d}T}\frac{\mathrm{d}T}{\mathrm{d}P}PNL \tag{2.31}$$

$$P = \frac{\lambda}{2NL} \frac{1}{\mathrm{d}n_{\mathrm{eff}}/\mathrm{d}T} \frac{1}{\mathrm{d}T/\mathrm{d}P}, \tag{2.32}$$

where $n_{\mathrm{eff}}$ is the effective index of the waveguides. Numerical simulations determined that $\frac{\mathrm{d}n_{\mathrm{eff}}}{\mathrm{d}T} \approx 1.93 \times 10^{-4}\ \mathrm{K}^{-1}$ for all of the waveguide widths used in this study.

First, the effect of the length of the suspended region was investigated. Figure 2.16 shows the simulated switching power, as a function of length, for a 12 $\mu$m wide suspended structure with 9 waveguides and various numbers of pairs of support bridges. It is clear that as the length of the device increases the switching power decreases dramatically. This is as expected since the rate of heat transfer via conduction along the suspended bridge is proportional to the gradient in temperature at its ends [70]. Therefore, if the characteristic length of the structure increases, then a larger change in temperature is required to dissipate the supplied power. Additionally, it can be seen that increasing the number of support bridges increases the required switching power. This is expected because the support bridges represent additional paths through which heat can be conducted away from the device.

Figure 2.17 shows the simulated switching power, as the width is varied, for example devices consisting of a 90 $\mu$m long device with no support bridges, and a 290 $\mu$m long device with two pairs of support bridges. For each width simulated, the number of waveguides was set to be the maximum number of waveguides that could be fit in the width with a 1 $\mu$m pitch, while keeping the waveguides at least 1 $\mu$m away from the edges of the suspended structure. To better visualize the trends for both examples simultaneously, the switching powers for each device are normalized to the switching power for that device with a 12 $\mu$m width.

For the case of the device with no bridges, it can be seen that there is only a very modest increase in switching power with increasing width. A simple argument suggests why this is the case. If heat loss is assumed to be dominated by conduction along the length of the suspended structure, rather than through convection to the air, then the rate of heat loss at a given temperature change is proportional to the cross-sectional area of the suspended structure, and in turn to the width. Thus the power required to get a given temperature change increases linearly with width. However, the number of waveguides that can fit in the structure also increases

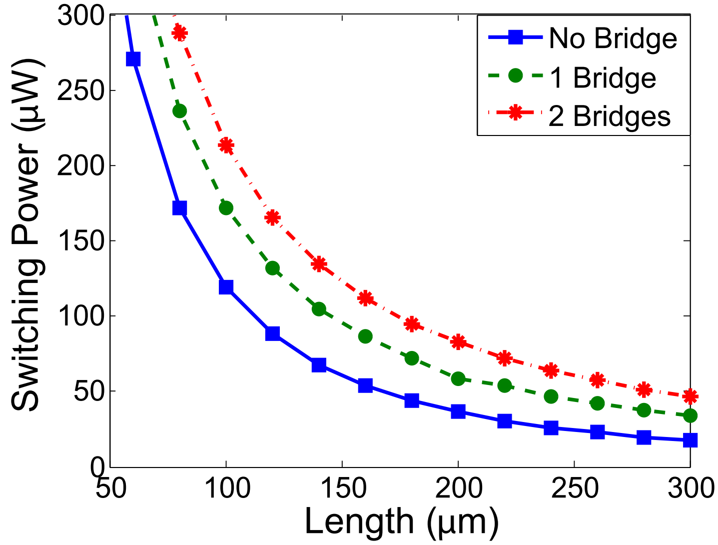


**Figure 2.16:** Switching power required for devices with 9 waveguides and varying number of support bridges.

linearly with width. Thus, equation 2.32 predicts that the switching power should be independent of width in this case.

On the the other hand, for the device with 2 pairs of support bridges there is a significant decrease of the switching power with width. This can be understood in much the same way as the decrease in switching power observed with increasing device length above, but applied to the heat lost due to conduction along the support bridges. As the width is increased, the average distance for heat to travel along to reach the support bridges is increased. Therefore, for a given temperature change, the rate of heat loss due to conduction along the support bridges is decreased. This observation shows that if support bridges are used, then a decrease in switching power can be achieved by increasing the suspended structure width. However, this comes at the expense of an increase in device footprint. In fact, a doubling of the structure width gives only a 25% reduction in switching power, so this trade-off is quite severe.

Figures 2.18 and 2.19 shows the temperature distributions for the 90 $\mu$m and 290 $\mu$m long devices, respectively. The normalized temperature change at a point

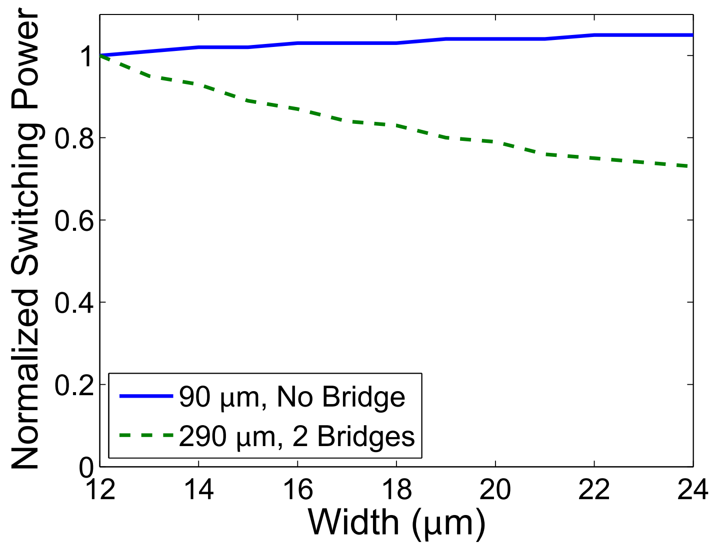


**Figure 2.17:** Normalized switching power required for devices as the width is varied. The number of waveguides for each width is the maximum number of waveguides that can fit within the structure with a 1 $\mu$m pitch.

is defined as the ratio of the temperature change at that point to the maximum temperature change in the structure.

To study the effect of underetching the silicon substrate, further simulations were performed for devices with the substrate not etched. First, the switching powers of the underetched and unetched versions of two example devices were calculated. For a 90 $\mu$m long, 12 $\mu$m wide device with 5 waveguides and no support bridges the simulated switching powers for the underetched and unetched versions were 6.1 mW an 0.26 mW, respectively. For a 290 $\mu$m long, 12 $\mu$m wide device with 5 waveguides and two pairs of support bridges, the simulated switching powers for the underetched and unetched versions were 3.4 mW and 0.14 mW, respectively. It is evident that the underetching results in a dramatic reduction in required switching power. This is due to the removal of the very efficient conduction path to the substrate with both a large area and short length.

Secondly, time domain simulations were carried out. The entire simulation vol-

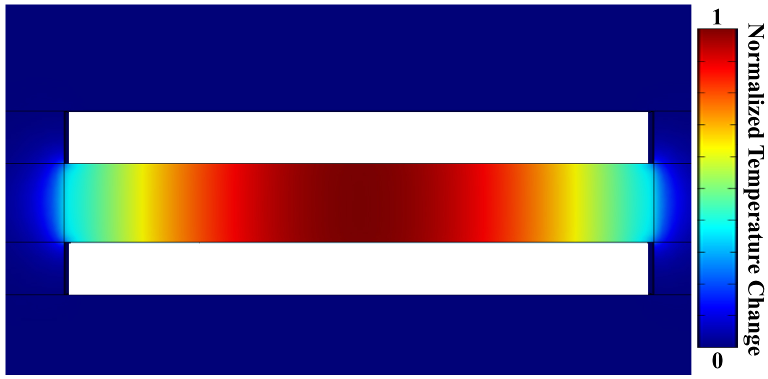


**(a)**

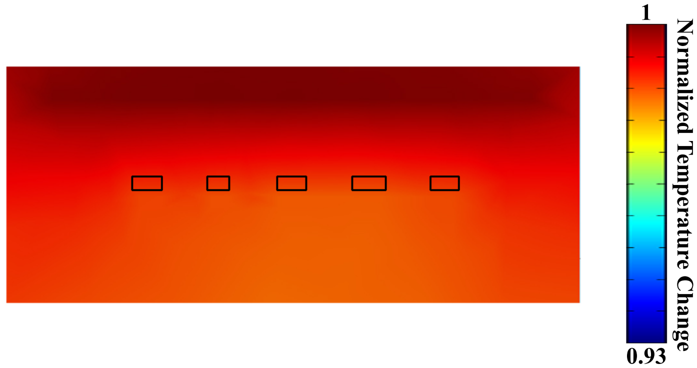


**(b)**

**Figure 2.18:** Temperature distribution in 90 $\mu$m long, 12 $\mu$m wide, suspended structure. a) overhead view, and b) cross-sectional view. Note the different scale in b). The black rectangles indicate the positions of the silicon waveguides.

ume was set to be the same temperature as an initial condition. The power supplied to the heater was then set to be 1 mW and the temperature change, averaged over the volume of the waveguides, was recorded as a function of time, $t$. The results for the unetched and underetched devices are presented in Figures 2.20 a) and b), respectively.

The difference in rise time between the long and short devices is much smaller for the unetched devices than for the underetched devices. To explain this observation it is helpful to explore the dynamics of heating and cooling. Provided that the

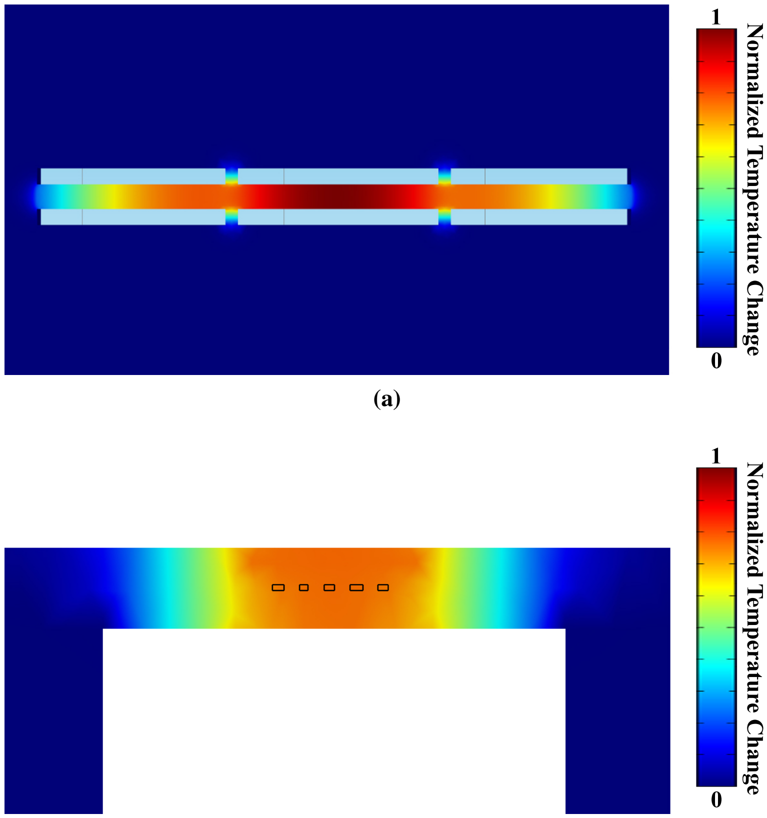


(b)

**Figure 2.19:** Temperature distribution in 290 $\mu$m long suspended structure with two pairs of support bridges. a) overhead view, and b) cross-sectional view in the center of one of the pairs of support bridges. The black rectangles indicate the positions of the silicon waveguides.

heat loss to conduction dominates over that due to convection, the rate of change of average temperature satisfies Newton's law of cooling [70],

$$C\frac{\mathrm{d}T}{\mathrm{d}t} = P - \dot{Q}, \tag{2.33}$$

where $C$ is the heat capacity of the structure, and $\dot{Q}$ is the rate of heat transfer away from the device. The heat capacity is proportional to the device volume, and thus to its length. $\dot{Q}$ is proportional to the temperature, relative to that of

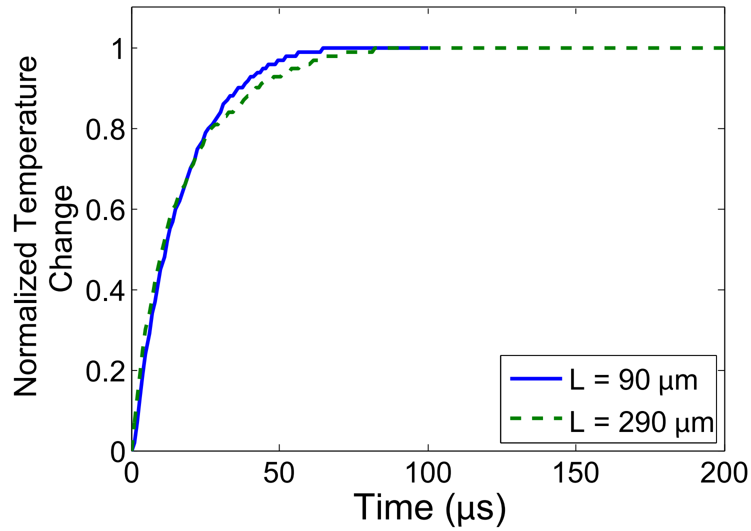


**(a)**

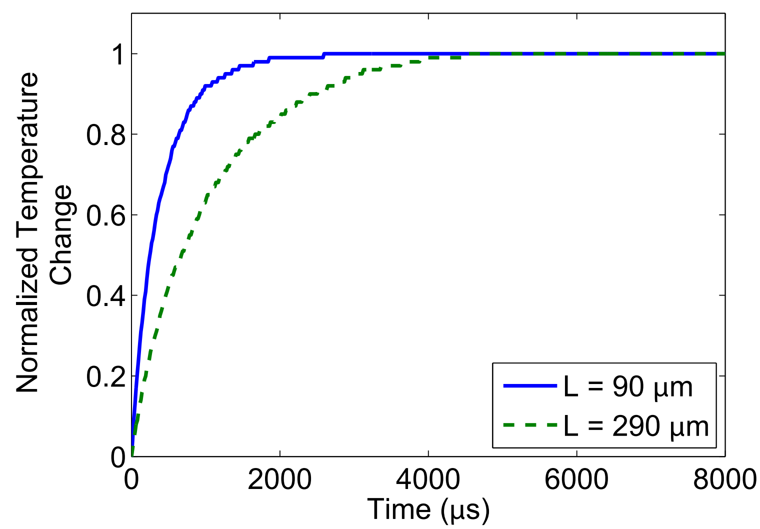


**(b)**

**Figure 2.20:** Finite element simulated time domain response of a) unetched and b) underetched heaters of different lengths. The 90 $\mu$m long device has no support bridges, and the 90 $\mu$m long device has two pairs of support bridges. A power of 1 mW is continuously supplied beginning at time 0.

the structure's surroundings, the cross-sectional area of the conduction pathways, $A_c$, and inversely proportional to the characteristic length, $L_c$, of the conduction pathways [70]. Thus, with appropriate proportionality parameters $a$ and $b$,which are material and geometry dependent, equation 2.33 can be written as

$$\frac{\mathrm{d}T}{\mathrm{d}t} = \frac{a}{L}(P - bA_cT/L_c). \tag{2.34}$$

To investigate the rise time, the rate of temperature change must be normalized to the maximum temperature reached, $T_{\max}$. Inspection of equation 2.34 gives $T_{\max} = PL_c/bA_c$, and in turn

$$\frac{1}{T_{\max}}\frac{\mathrm{d}T}{\mathrm{d}t} = \frac{Pa}{LT_{\max}}(1 - T/T_{\max}). \tag{2.35}$$

Solving equation 2.35 for an initial temperature of $T = 0$, relative to the temperature of the surroundings, gives the solution

$$\frac{T}{T_{\max}} = 1 - e^{-t/\tau_c} \tag{2.36}$$

$$\tau_c = \frac{LL_c}{abA_c}, \tag{2.37}$$

where $\tau_c$ is the characteristic rise time of the structure, giving the time required for the temperature change to reach $1 - 1/e \approx 63\%$ of its maximum.

Using equation 2.36, one can explain the observations made above about the results in Figures 2.20 a) and b). For the case of the unetched devices the primary conduction path for heat transfer is expected to be directly to the substrate through the botttom of the glass structure. Thus we can identify the area of this surface with $A_c$, and find that it is proportional to the structure length. As for the characteristic length for this conduction pathway, it can be identified with the thickness of the glass structure, which is independent of the device length. Combining these observations, and equation 2.4, one can see that the rise time can be expected to be independent of the device length. This is consistent with the simulation results. For the underetched devices, however, the dominant conduction pathways are expected to be through the ends of the suspended structure and along the support bridges, if present. The characteristic area $A_c$ can then be associated with the sum of cross-sectional areas of the glass structure and of the support bridges, if present. The characteristic length would then be expected to be proportional to the physical length of the structure. Thus, the rise time would be expected to scale proportionally to $L^2/A_c b$. Since the $b$ parameters for the geometries where bridges are and are not present are unknown, this cannot be used to evaluate a predicted ratio for the rise times to compare with the simulation. However, it does make the useful prediction that for underetched devices the rise time can be expected to scale with the square of length.

Substituting the expression for $T_{\max}$ into equation 2.32, in combination with the scaling arguments presented above for the underetched and unetched devices, gives predictions for the scaling behaviour of the switching power. Specifically, the switching power of unetched devices is predicted to be independent of length, and the switching power of underetched devices is predicted to scale as $L^{-2}$. A power law fit to the simulated switching power results for the underetched device with no bridges in Figure 2.16 as a function of length gives good agreement with a $L^{-1.7}$ dependence. The discrepancy between this result and the predicted $L^{-2}$ dependence is most likely due to the neglect of the effects of convection in equation 2.32 because the influence of convection, relative to that of conduction, can be expected to increase with device length.

With the above predicted scaling behaviour of the rise time and switching power of unetched and underetched devices we can define a figure of merit for comparing the performance of devices when both speed and efficiency are concerns. Considering the product of rise times and switching powers, the above analysis gives that this quantity is predicted to be independent of length for both unetched and underetched devices. Based on this, the proposed figure of merit, FOM is defined as

$$\mathrm{FOM} = \tau_c P_\pi \tag{2.38}$$

where $P_\pi$ is the switching power. This is the same figure of merit used in [34]. Of course, convection is neglected in the analysis above so the predicted scaling behaviour will not be exact. Therefore the figures of merit should be taken as a rough comparison metric and not as a definitive predictor of relative performance.

## 2.5 Chapter Summary and Conclusions

In this chapter an overview of the structure and operating principle of an MZI-based switch was first presented. The remainder of the chapter was devoted to the development of models of the optical, mechanical, and thermal properties of suspended folded waveguide structures.

An optical model based on coupled mode theory was used to predict the transmission through folded waveguide structures with either identical or dissimilar waveguides. The ripple in the through spectrum of the structure was shown to be an appropriate metric for evaluating the extent of crosstalk present, and it was predicted that a higher waveguide density could be achieved, while maintaining low crosstalk, with dissimilar waveguides than with identical waveguides. A path integral model of the folded waveguide structure was also developed, which provides an intuitive picture for discussing and visualizing how light propagates in a folded waveguide structure when coupling is present. The analogy between the folded waveguide structure and quantum mechanical systems was discussed, and it was determined that the analagous systems are not physically relevant.

A mechanical model of the structure was used to simulate the stress distribution in a suspended waveguide structure under a uniform acceleration. It was found that, for devices with reasonable cross-sectional dimensions, the suspended structure likely only needs to be supported at its ends (*ie.*, it does not need support bridges) for lengths up to 300 $\mu$m. The addition of support bridges further increases the mechanical stability as expected.

A thermal model of the folded waveguide structure was used to predict the switching power and switching speed for devices using different designs, both for unetched and underetched devices. In addition to simulations, simple theoretical considerations were used to predict the scaling behaviour of the switching power and switching speed with variations of the width or length of the structure. The predicted scaling dependencies were used to propose a figure of merit, which quantifies the tradeoff between switching power and switching speed, for both unetched and underetched devices. It was found that to minimize the switching power, one should design an underetched device that is long and has no support bridges.

# Chapter 3

# Device Design and Experimental Investigation

## 3.1 Device Design

### 3.1.1 A 2×2 Switch

Figure 3.1 a) shows a schematic diagram of the fabricated devices. Input light is split by a 50-50 adiabatic splitter [53] and the light traveling along one of the MZI arms passes $N$ times through the thermal phase shifter before recombining with the light from the other arm at the device output. Figures 3.1 c) and d) show the cross-section of the phase shifter region for unetched and underetched devices, respectively. Each of the $N$ waveguides has a thickness of 220 nm, a width, $w_i$, $i = 1, 2, \ldots, N$, and all waveguides are separated by a common gap, $g$. A 10 $\mu$m wide heater of length $L$ is used to apply a temperature change to the waveguides to induce a thermo-optic phase shift. In the case of the underetched devices, the silicon substrate has been removed to form a 12 $\mu$m wide suspended bridge to increase thermal isolation. The devices were fabricated using 248 nm optical lithography at the Institute of Microelectronics (IME), Singapore. The unetched and underetched versions of the device were measured from different wafers. Figure 3.1 b) shows an optical image of a fabricated device.

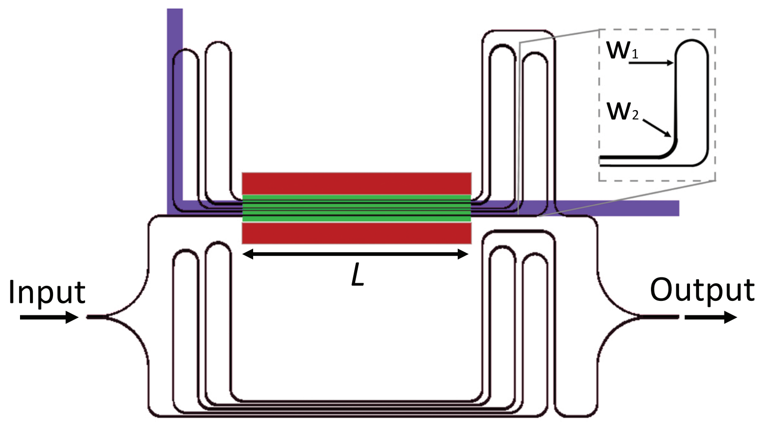
W1
W2
L
Input
Output

**(a)**

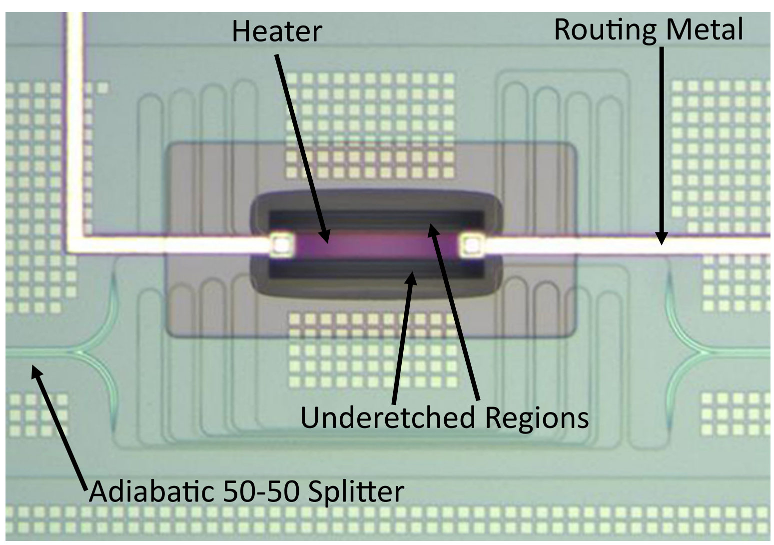
Heater
Routing Metal
Underetched Regions
Adiabatic 50-50 Splitter

**(b)**

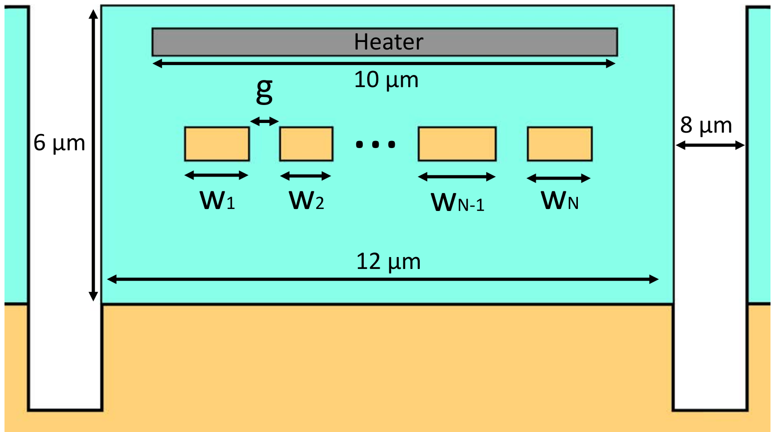


**(c)**

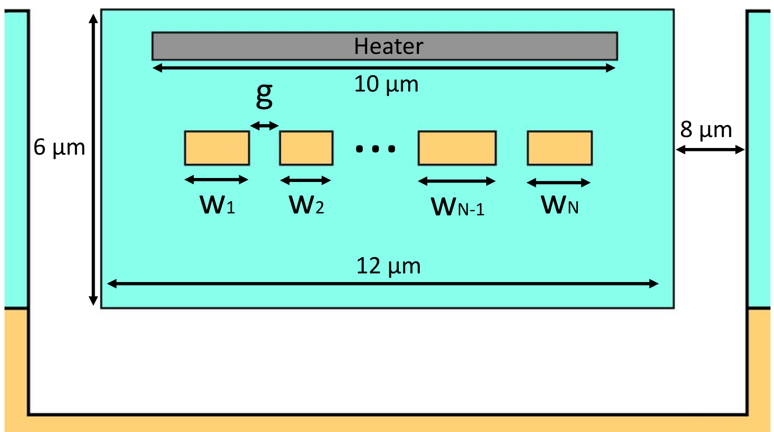


**(d)**

**Figure 3.1:** a) Schematic of thermally tunable MZI switch. Black traces: WGs, Red: Oxide openings define underetched region, Purple: Routing metal, and Green: Heater metal. Inset: Waveguide taper region. b) An optical micrograph of a fabricated device. c) Thermal phase shifter cross-section before underetching. d) Thermal phase shifter cross-section after underetching. In c) and d), silicon dioxide is blue, silicon is tan, the metal heater is grey, and air is white. ©Optical Society of America, 2015, by permission.

**Table 3.1:** Device parameters

| | Device 1 | Device 2 | Device 3 | Device 4 | Device 5 |
|---|---|---|---|---|---|
| $N$ | 3 | 5 | 5 | 9 | 9 |
| $w_i$ (nm) | 500, 500<br>500 | 500, 400<br>550, 650<br>500 | 500, 400<br>550, 650<br>500 | 500, 600, 400<br>550, 650, 450<br>600, 400, 500 | 500, 600, 400<br>550, 650, 450<br>600, 400, 500 |
| $g$ ($\mu$m) | 3.0 | 1.0 | 1.0 | 0.5 | 0.5 |
| $L$ ($\mu$m) | 120 | 90 | 290 | 90 | 290 |

Five different devices were fabricated to study the effect of dense dissimilar waveguide routing on the tuning efficiency of MZI switches. Device 1 was used as a baseline device using identical waveguides and a gap of 3 $\mu$m to ensure no degradation of the spectrum due to crosstalk. Devices 2 and 3 used dissimilar waveguide routing with a gap of 1 $\mu$m, and devices 4 and 5 used dissimilar waveguides with a gap of 0.5 $\mu$m for the most dense routing. Devices 3 and 5 included two pairs of support bridges with a 6 $\mu$m width and 8 $\mu$m length. Table 3.1 summarizes the parameters of each device. The widths of the waveguides were picked such that adjacent waveguides have a width difference of at least 100 nm and next-to-adjacent waveguides have a width difference of at least 50 nm to protect against any effect of non-nearest neighbour coupling that was not considered in the theoretical analysis [50]. Device 1 was fabricated only in an unetched configuration while devices 2-5 were fabricated in both unetched and underetched configurations. The footprints of device 1, devices 2 and 4, and devices 3 and 4 were approximately 650 $\mu$m $\times$ 180 $\mu$m, 600 $\mu$m $\times$ 180 $\mu$m, and 800 $\mu$m $\times$ 180 $\mu$m, respectively.

### 3.1.2 A 4×4 Switch

Figure 3.2 shows a schematic of a 4×4 switch composed of the switch elements described above. The switch architecture is the non-blocking switch described in [71]. In addition to the switching elements, the waveguide crossings described in

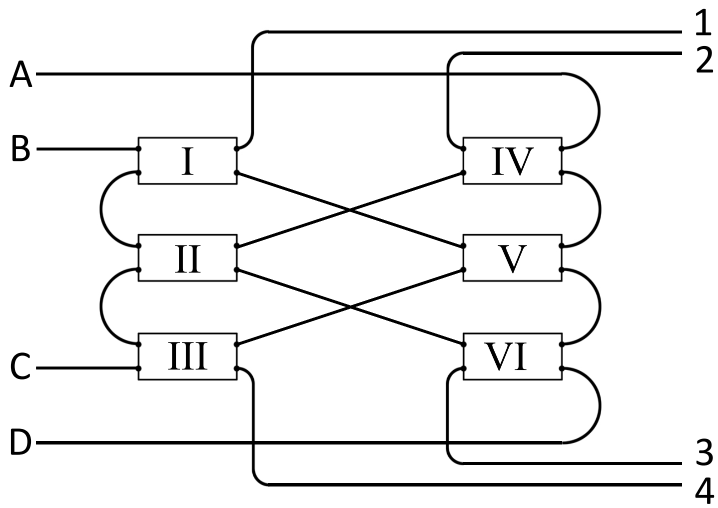


**Figure 3.2:** A schematic of a 4×4 switch. The 2×2 switches I through VI route light from the inputs A,B,C, and D to the outputs 1,2,3, and 4.

[72] are utilized during routing waveguides between the switches. Due to space constraints, only one 4×4 switch could be fabricated and so the underetched version of device 5 was used to create the switching elements. Device 5 was chosen to achieve the lowest switching power. By thermally actuating the switches I through VI it is possible to route light from any of the input ports, labelled by the letters A-D, to any of the output ports, labelled by the numbers 1-4. Table 3.2 gives the tuning states required of each of the switches for each routing state. The tuning states given are examples only, as the tuning states of the switches are in general not unique.

## 3.2 Experimental Procedure

A schematic of the experimental test setup is shown in Figure 3.3. A tunable laser source was used to inject 0 dBm of light through an optical fiber into the chip through TE grating couplers [73]. After passing through a device the light exited the chip through a second fiber grating coupler and the transmitted light was passed to a photodetector. The wavelength of the input light was swept from 1530 nm to 1580 nm in 0.1 nm steps and the transmission spectrum of the device was recorded.

**Table 3.2:** Switch routing states

| In\Out | 1 | 2 | 3 | 4 |
|---|---|---|---|---|
| A | 10X1XX | XXX0XX | X10101 | XX111X |
| B | 0XXXXX | 1XX10X | 1XXX11 | 11100X |
| C | 111X00 | XX111X | XX1X01 | XX0XXX |
| D | 11XXX1 | X00111 | XXXXX0 | X01XX1 |

The characters represent the tuning state of switches I through VI in order. 0 is the through state, 1 is the cross state, and X indicates that the state of a switch does not matter.

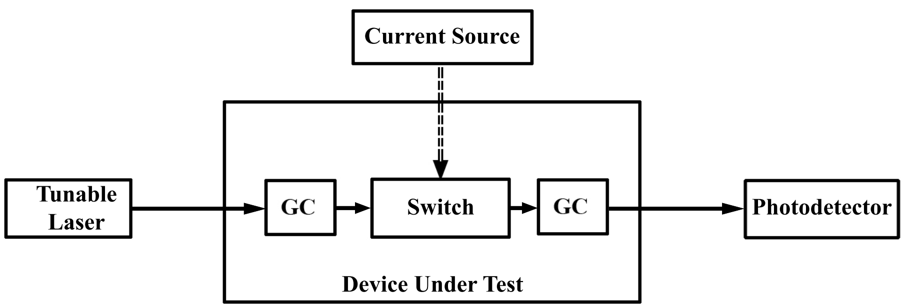


**Figure 3.3:** A schematic diagram of the experimental setup. Solid and dashed lines indicate optical and electrical connections, respectively.

This procedure was repeated while applying several different current levels to the phase shifter heaters and recording the power supplied. Additionally, the adiabatic splitters used to form the interferometers were characterized by injecting light into one of their input ports and simultaneously measuring the transmission to their output ports through TE grating couplers.

## 3.3 Results and Discussion

Figure 3.4 a) shows a schematic of the adiabatic splitter used to form the MZI, and 3.4 b) shows the measured transmission through the structure. It can be readily

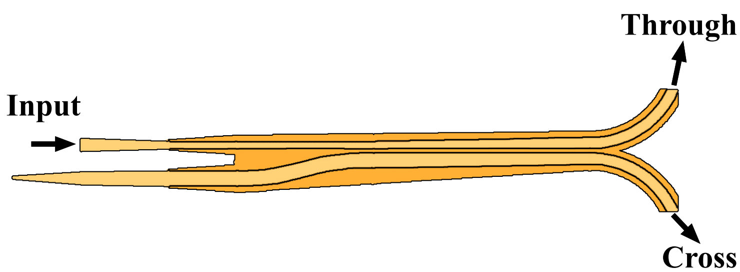


**(a)**

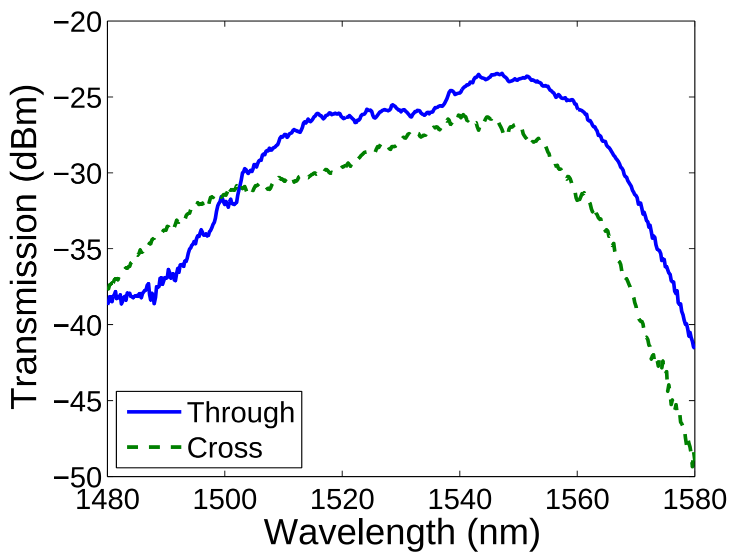


**(b)**

**Figure 3.4:** a) A schematic of the adiabatic splitter. The tan is 200 nm thick silicon, and the orange is 90 nm thick silicon slab. b) Measured transmission through an adiabatic splitter.

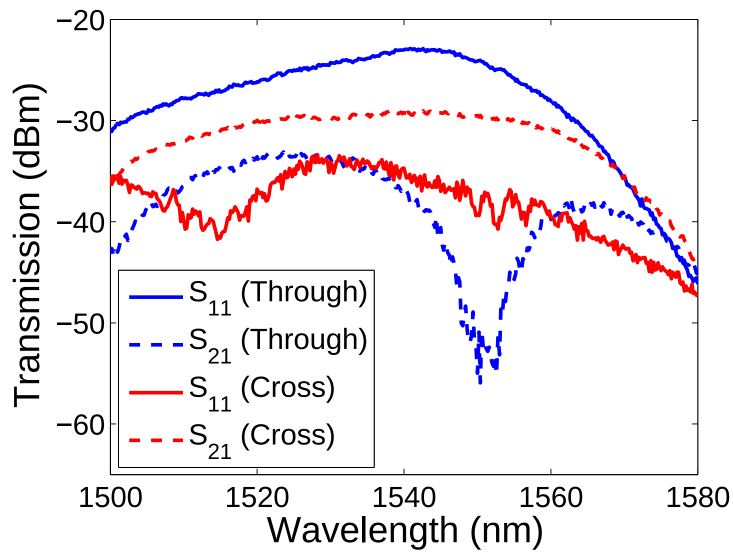


**Figure 3.5:** Transmission to the two output ports of an implementation of device 2 in the through and cross states. The numbers 1 and 2 indicate the upper and lower arms, respectively, of the switch input and output.

seen that the splitting ratio is both far from 50-50 and strongly wavelength dependent. Since the measured splitting ratio in [53] was good for the same design, this suggests that there may have been a significant fabrication error in producing the splitter. Similar performance was measured on several chips.

Despite the poor splitting ratio measured, the transmission of a switch was investigated to determine if the efficiency of the phase shifters could still be extracted. Figure 3.5 shows the transmission of an implementation of device 2. The through state is defined as the state of the switch where the power supplied to the phase shifter is such that when light is injected into the upper arm of the input splitter, the transmission to the upper arm of the output splitter, $S_{11}$, is maximized. Similarly, the cross state is the state where the power supplied to the phase shifter is such that the transmission from the upper arm of the input splitter to the lower arm of the output splitter, $S_{21}$, is maximized. It can be seen that the extinction ratio for through operation, $S_{11}(\text{Through})/S_{11}(\text{Cross})$, is much less than the extinction ratio for cross operation, $S_{21}(\text{Cross})/S_{21}(\text{Through})$. Similar behaviour was observed in all devices tested. The poor performance in through operation is most likely due to the unequal splitting by the adiabatic splitters. Thus, for all subsequent testing the switches were tested for cross operation and the on state refers to the cross state, while the off state refers to the through state.

In all cases the extinction ratio of the switch was measured to be greater than 20 dB. Figures 3.6 a) and 3.6 b) show example optical spectra of the underetched versions of devices 3 and 5, respectively, in the on and off state. It can be seen that even for the longest devices tested the more aggressive waveguide routing density of device 5 compared to device 3 has not had a negative effect on either the extinction ratio of the switch or the ripple in the transmission spectrum, which is maintained at below 0.1 dB peak to peak. This suggests that the dissimilar waveguides have successfully prevented cross-coupling of power in the dense routing regions of the switch. The insertion losses of the switches were estimated to be -0.9 dB, -1 dB, -2.5 dB, -1.2 dB, and -2.9 dB for devices 1-5, respectively. The difference in insertion loss is due to the difference in propagation loss for the different arm path lengths. The insertion loss was found not to depend on whether or not the device was underetched. The envelope of the transmission spectrum in the on state is due to the wavelength-dependent coupling efficiency of the grating couplers used [73]. The wavelength dependence of the extinction ratio is due to an optical length mismatch between the two arms, which is likely due to variations in the thickness of the silicon layer across the wafer [74], as well as due to the wavelength dependence of the splitter splitting ratio. The period of the variations in extinction ratio could be extended to create a more broadband device by designing a switch such that the average distance between its arms is smaller, at the expense of an increased thermal crosstalk between the arms.

Figure 3.7 show the normalized transmission functions of the unetched and underetched versions of devices 2-5 as functions of the power applied to the thermal phase shifter, along with sinusoidal fits to the data. The wavelength of operation was 1550 nm. It can be seen that in all cases the devices with more dense waveguide routing give higher phase shifter efficiency. The measured efficiencies are given in Table 3.3, along with the efficiencies simulated as described in Section 2.4. It can be seen that the relative improvement in phase shifter efficiency when increasing waveguide routing density is greater for short devices than for long de-

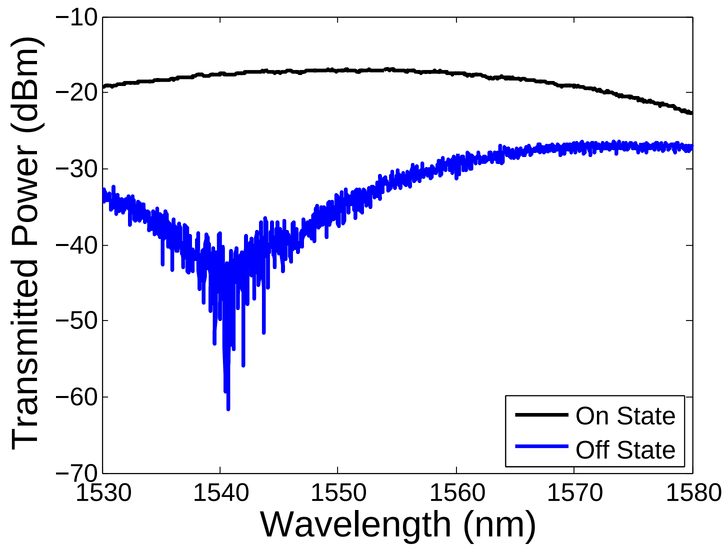


**(a)**

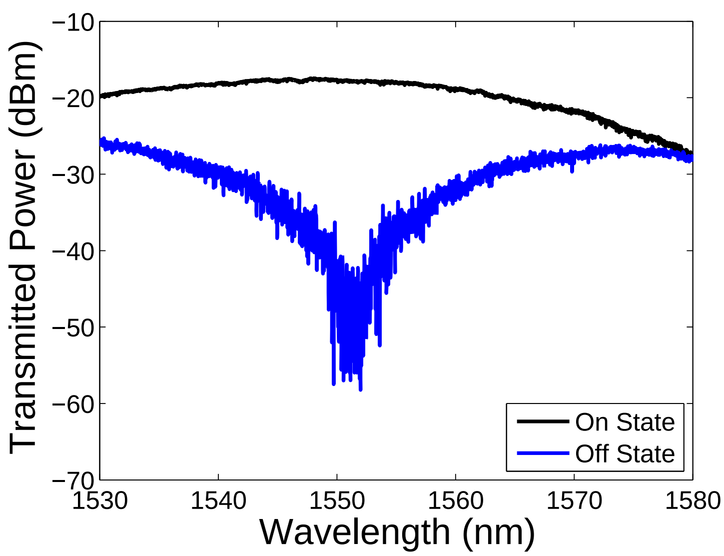


**(b)**

**Figure 3.6:** Measured spectra of the underetched versions of a) device 3 and b) device 5. ©Optical Society of America, 2015, by permission.

**Table 3.3:** Tuning efficiency of MZI switches (mW/$\pi$)

| | Device 1 | Device 2 | Device 3 | Device 4 | Device 5 |
|---|---|---|---|---|---|
| Measured Unetched | 14 | 8.7 | 5.9 | 3.8 | 4.2 |
| Measured Underetched | N/A | 0.68 | 0.16 | 0.20 | 0.095 |
| Simulated Unetched | 10 | 6.1 | 5.9 | 3.4 | 3.3 |
| Simulated Underetched | N/A | 0.26 | 0.09 | 0.14 | 0.048 |

vices, and that the ratio of efficiencies approaches the ratio of waveguide densities for the long devices. Further, the relative change in efficiency when increasing waveguide routing density is similar for both the unetched and underetched devices. The highest efficiency achieved, 95 $\mu$W/$\pi$, is to the best of our knowledge the highest efficiency reported to date for thermally actuated MZI switches. It can be seen that the simulated efficiencies generally agree with the measured values more closely for the unetched devices than for the underetched devices. The trends in the measured data, however, are well captured despite a consistent underestimation of the efficiencies. One possible explanation of this observation is that the simple model of convection used is not sufficient to accurately describe the heat loss to the air, which is expected to be more important for underetched devices than for unetched devices. The fact that the model correctly predicts the relative performance of the different devices suggests that the results of the simulation can nevertheless be a useful tool to make predictions about the relative performance of potential future designs.

Figure 3.8 shows the temporal response of the MZI switches when the heaters were driven with a square pulse. The temporal response was found not to depend significantly on the waveguide routing density, but only on the heater length and whether or not the device was underetched. This suggests that the increase in device efficiency with increasing waveguide density does not come at the expense of a slower response time. The measured response times are summarized in Table 3.4, along with the rise times simulated as described in Section 2.4. Simulated fall times are not included, as they are expected to be the same as the rise times due to the linearity of the thermal model used. It is clear that the increases in efficiency

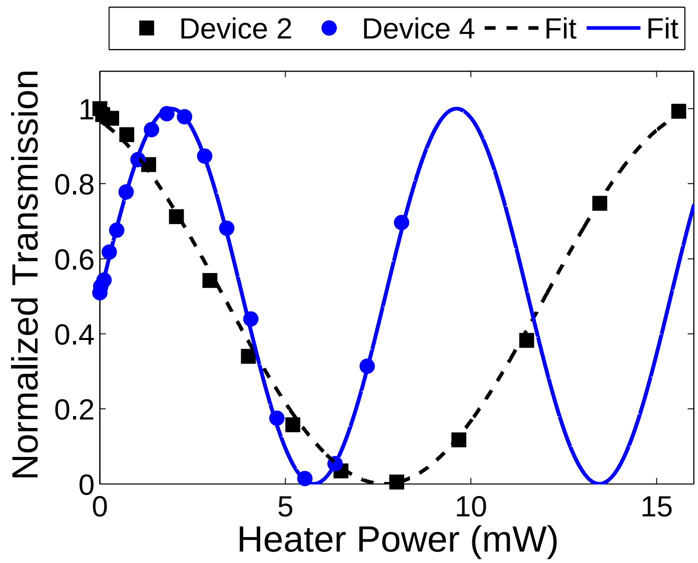
Device 2
Device 4
Fit
Fit
Normalized Transmission
0
0.2
0.4
0.6
0.8
1
0
5
10
15
Heater Power (mW)

**(a)**

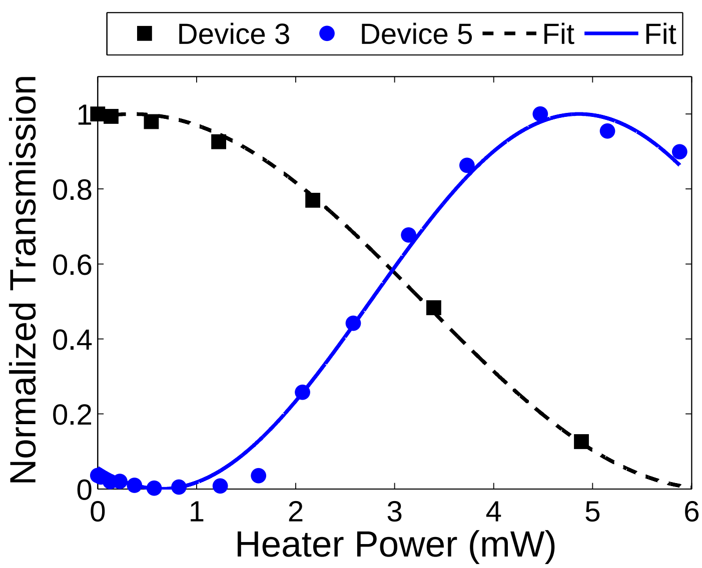
Device 3
Device 5
Fit
Fit
Normalized Transmission
0
0.2
0.4
0.6
0.8
1
0
1
2
3
4
5
6
Heater Power (mW)

**(b)**

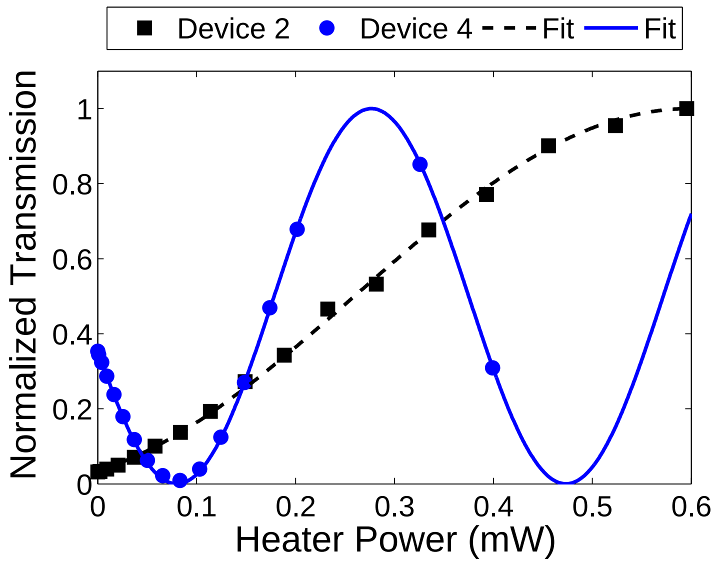


**(c)**

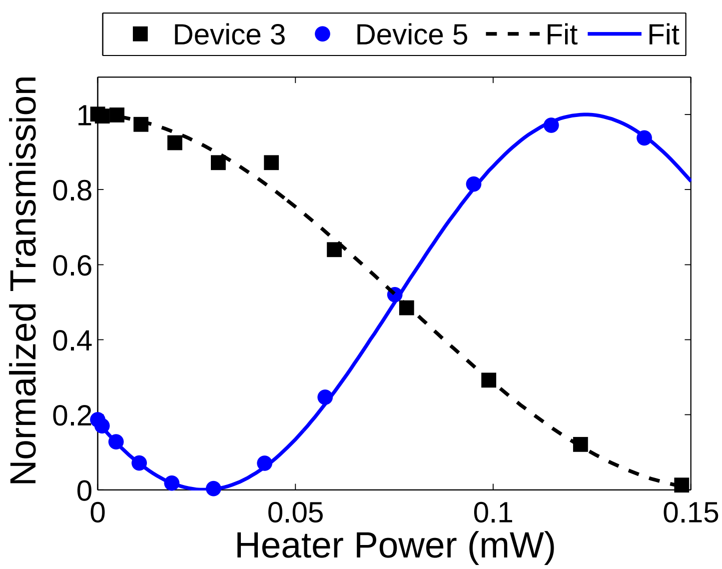


**(d)**

**Figure 3.7:** Normalized transmission functions of the a) short (devices 2 and 4) unetched, b) long (devices 3 and 5) unetched, c) short underetched, and d) long underetched MZI switches. ©Optical Society of America, 2015, by permission.

**Table 3.4:** 10-90 Response times of MZI switches ($\mu$s)

| | Unetched Device 3 | Unetched Device 5 | Etched Device 3 | Etched Device 5 |
|---|---|---|---|---|
| Measured Rising | 40 | 60 | 550 | 750 |
| Measured Falling | 45 | 65 | 550 | 1200 |
| Simulated Rising | 35 | 45 | 930 | 2400 |

when underetching devices or increasing device length come with an increase in the response time due to the improved thermal isolation of the heated region from its environment. Further, it can be seen that the simulated response times give agreement with the measured data similar to the agreement achieved between the simulated and measured phase shifter efficiencies in Table 3.3. Like in Table 3.3, the agreement between measurement and simulation is better for the undetched devices than for the underetched devices. Again, we suggest that this may be due to the simple model of convection used and point out that the relative performance of the devices can be accurately predicted through simulation. The observed difference between the observed rise and fall times in the experimental results cannot be explained by the linear thermal model in Section 2.4. One possible explanation of the difference observed is that the change in intensity is not proportional to the change in device temperature due to the non-linear change in the transmission of an MZI when a phase shift is introduced. Thus, for large phase shifts one can expect to see deviations from the linear model in Section 2.4. This, of course, can also explain some of the discrepancy between the simulated rise times and the experimental values.

Table 3.5 shows the calculated and simulated figures of merit for the unetched and underetched versions of a short and a long device. For both the long and short devices, the device with higher waveguide density was chosen to evaluate the figure of merit because, having lower switching power and similar response times as compared to the less dense waveguide versions, they are expected to have lower figures of merit. Two observations about the data should be noted. The first is that the agreement between the simulated values and the predicted values

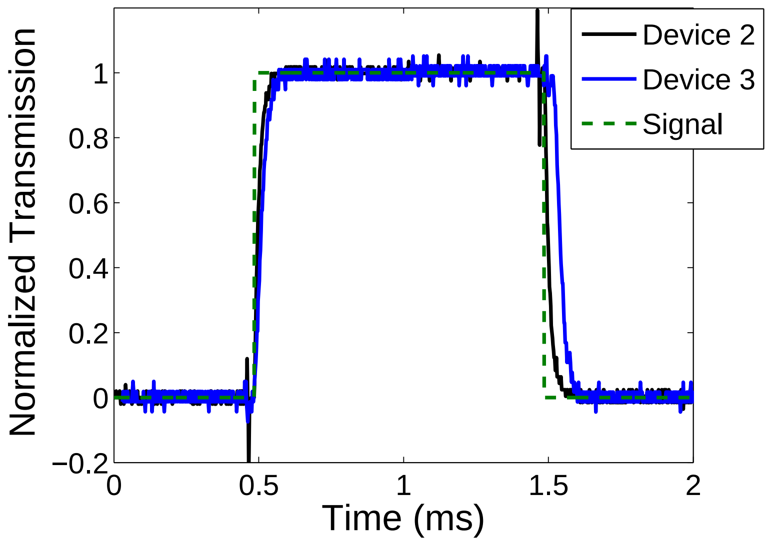


**(a)**

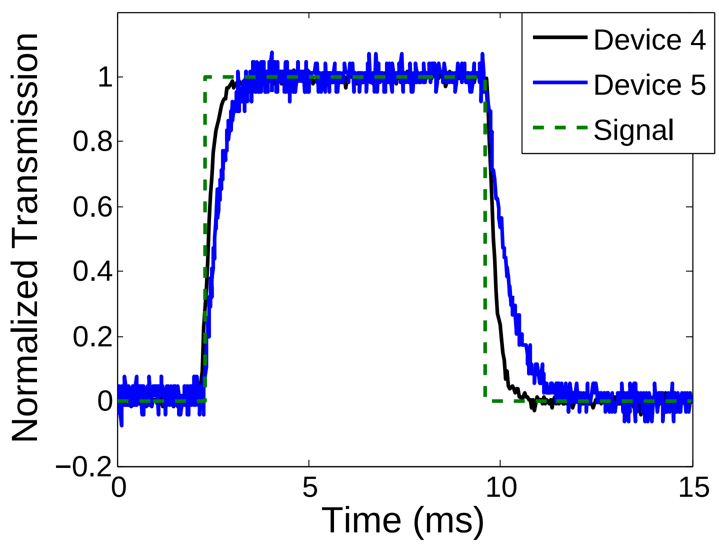


**(b)**

**Figure 3.8:** Temporal response of a) unetched, and b) underetched MZI switches. ©Optical Society of America, 2015, by permission.

**Table 3.5:** Figures of merit of MZI switches (nJ)

| | Unetched Device 3 | Unetched Device 5 | Etched Device 3 | Etched Device 5 |
|---|---|---|---|---|
| Measured FOM | 102 | 110 | 41 | 30 |
| Simulated FOM | 90 | 65 | 37 | 50 |

for the underetched devices is generally better than said agreement for either the switching powers or response times individually. This is because the underestimate in simulated switching power was counteracted by an overestimate in response time. Secondly, it can also be seen that the agreement between the simulated and measured values is generally better for the short devices than for the long devices. This observation is consistent with the hypothesis that conduction is being poorly modelled because, since convection is expected to contribute more to the heat loss relative to conduction as the device length is increased, this inaccuracy should be expected to cause a greater discrepancy for longer devices.

Figures 3.9 a), b), and c) show comparisons of the performance of the underetched version of device 5, in terms of switching power, $P_\pi$, characteristic rise time, $\tau_c$, and the figure of merit $P_\pi \tau_c$, respectively, with previously reported experimental results [2]. When only 10-90 rise times were given, the characteristic rise time was estimated using the single pole temporal response described by equation 2.36. It can be seen in Figure 3.9 a) that the two results related to this thesis, [1] and [2], have, by utilizing dissimilar waveguides, achieved significantly lower switching powers than previously reported results. The result in [2] was achieved by utilizing a similar phase shifter design to that of the underetched version of device 5 in this thesis in a Michelson interferometer, similarly to the device in [23]. In a Michelson interferometer, the light passes through a phase shifter twice, and therefore requires half the switching power as compared to an MZI utilizing the same phase shifter. Despite achieving such low switching powers, these devices have response times that are lower than some devices with significantly higher switching powers, as is shown in Figure 3.9 b). This observation suggests that the devices in this work demonstrate a good tradeoff between switching power and response time. This is

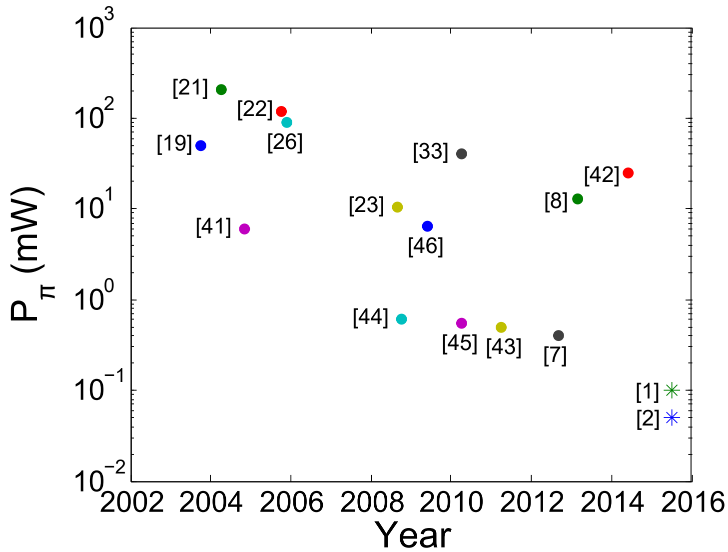

$10^3$
$10^2$
$10^1$
$10^0$
$10^{-1}$
$10^{-2}$
$P_\pi$ (mW)
[21]
[22]
[26]
[19]
[33]
[42]
[8]
[23]
[41]
[46]
[44]
[45]
[43]
[7]
[1]
[2]
2002 2004 2006 2008 2010 2012 2014 2016
Year


**(a)**

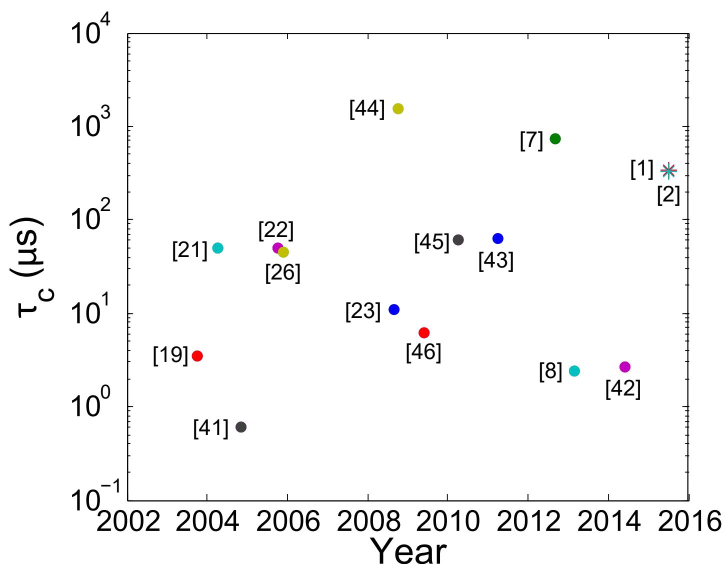

$10^4$
$10^3$
$10^2$
$10^1$
$10^0$
$10^{-1}$
$\tau_c$ (µs)
[44]
[7]
[1]
[2]
[22]
[21]
[26]
[45]
[43]
[23]
[46]
[19]
[8]
[42]
[41]
2002 2004 2006 2008 2010 2012 2014 2016
Year


**(b)**

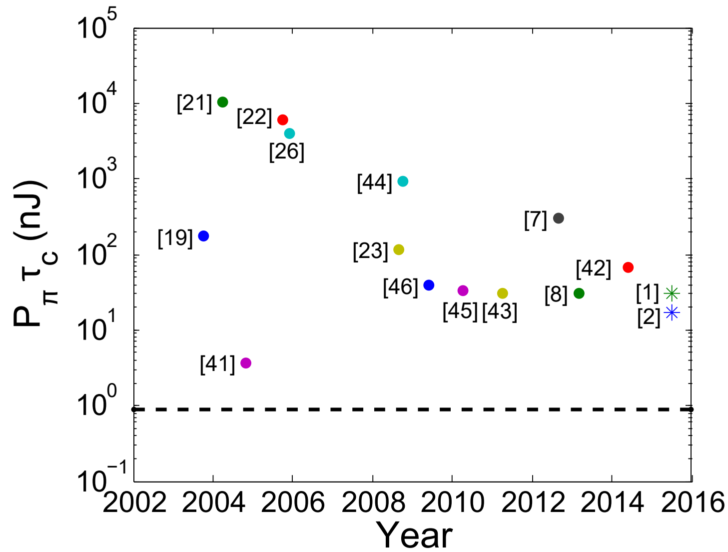


**(c)**

**Figure 3.9:** Comparisons of the a) switching powers, b) characteristic rise times, and c) figures of merit of thermo-optic switches over the past decade. The asterisk markers represent works related to this thesis.

supported by the results in Figure 3.9 c), which show that the figure of merit of the device in this work is competitive with the lowest figures of merit of recent results. Given the derivations in Section 2.4 showing that the figure of merit is independent of length, what is the source of the large difference between the figures of merit in the literature? The efficiency of heating, in terms of the amount of power that goes towards heating the waveguides as compared to the amount of power that heats their surroundings, is the main differentiator. For example, for the devices utilizing folded waveguides in a suspended structure, the volume of the waveguides as compared to the total volume of the suspended structure is greater by approximately a factor of the number of waveguides when compared to a suspended structure of the same size using only one waveguide. This observation can be used to compute an estimated lower bound on the figure of merit for silicon waveguides as described in Appendix B. This lower bound is plotted in Figure 3.9 c) for comparison. The fact that all of the observed values are much greater than the lower bound suggests that there is room for improvement. The primary way to improve the design of the structure in this regard would be to reduce the thickness of the glass in the suspended structure so that less heat is wasted heating the glass. Reduction in the thickness of the glass is, however, limited by the need for the metal heater to be sufficiently far away from the waveguides.

When measuring the 4×4 switch shown in Figure 3.2, the currents supplied to the relevant 2×2 switches for each routing state, as detailed in Table 3.2, were varied to obtain either the maximum or the minimum transmission. Due to the poor performance of the 2×2 switches in through operation as described above, the extinction ratios between the on and the off state were as low as 5 dB for routing between some ports. This very poor performance lead to not further investigating the performance of the 4×4 switch. Due to space constraints during fabrication, only one 4×4 switch could be fabricated, and therefore there were no switches fabricated utilizing different types of 3 dB splitters, such as multimode interferometer splitters [75], which may have given superior performance.

## 3.4 Chapter Summary and Conclusions

In this chapter, the designs of fabricated switches were described, the experimental procedure used for testing was outlined, and the experimental results were presented, compared to results predicted through simulation, and discussed.

Five $2 \times 2$ switch designs were fabricated in both unetched and underetched configurations to evaluate the impact of waveguide density and thermal isolation on the performance of the devices. All of the switches utilized adiabatic 3 dB splitters to form an MZI for testing purposes. The 3 dB splitters were found to have a poor splitting ratio, and so the interferometers only performed well in switching light intensity at one of their output arms.

It was experimentally shown that the increase in waveguide routing density near a heating element achievable by using dissimilar waveguides can be an effective way to improve the efficiency of thermal phase shifters for both undetched and underetched devices. The switching power was found to be greatly reduced both by underetching to form suspended structures and by increasing the density of waveguides in the heated region. Although the dramatic reduction in switching power with underetching came with a correspondingly large increase in switch response time, there was no such tradeoff observed by increasing the waveguide density. All of the $2 \times 2$ switches fabricated exhibited extinction ratios greater than 20 dB, and ripple in the through spectrum of less than 0.1 dB, showing that routing with dissimilar waveguides can effectively suppress crosstalk for even highly agressive waveguide densities.

The agreement of the simulated switching powers and times of the devices with the measured values was better for the unetched devices than for the underetched devices, but the simulations correctly predicted the trends in the data and the relative performance of the devices.

The highest efficiency phase shifter fabricated, the underetched version of device 5, was found to require 4 times less switching power than the highest efficiency thermo-optic MZI switch reported to date. Further, this phase shifter demonstrated a figure of merit competitive with previously reported results, indicating that the device achieves a good tradeoff between switching power and response time.

A $4 \times 4$ switch was also analysed and fabricated. Due to the poor splitting ratio of the 3 dB splitters used, however, the $4 \times 4$ switch's performance was poor and was not characterized in depth.

# Chapter 4

# Conclusions and Suggestions for Future Work

## 4.1 Summary and Conclusions

Theoretical models and finite element simulations were used to predict the performance of thermo-optic switches based on folded waveguide structures utilizing dense dissimilar waveguides. The dependence of the performance, as characterized by amount of crosstalk, switching power, switching time, and mechanical stability, on key device parameters was evaluated. The amount of ripple in a switch's through spectrum was proposed as an appropriate measure of switch crosstalk, and a figure of merit for quantifying the tradeoff between switching power and switching speed was proposed. The limitations of the figure of merit for device comparisons were discussed. It was experimentally shown that the increase in waveguide routing density near a heating element achievable by using dissimilar waveguides can be an effective way to improve the efficiency of thermal phase shifters for both unetched and underetched devices. Since the increase in device efficiency comes at the expense of a slower response, in applications requiring faster operation it is not desirable to achieve the highest efficiency possible at the expense of speed. In large switch networks, however, the power required for switching scales with the number of switches in the network while the switching speed is independent of the number of switches since the switches can be switched simultaneously. Thus, as the size of switch networks increases it becomes increasingly important to design devices to be no faster than required so as to minimize power consumption. The thermal models developed here can be used to guide the design of switches in this regard. Utilizing highly dense routing of 9 waveguides under a 10 $\mu$m wide heater allowed us to fabricate an MZI switch with ultra-low switching power of 95 $\mu$W, while maintaining an extinction ratio greater than 20 dB and ripple in the through response of less than 0.1 dB. The waveguide routing density was found to not impact the switch response time, and the switch demonstrated a good tradeoff between switching power and response time, competitive with the performance of previously reported devices. The device footprint was less than 800 $\mu$m $\times$ 180 $\mu$m.

## 4.2 Suggestions for Future Work

Theoretical considerations suggest some techniques that could be used to further increase the efficiency of the phase shifters designed in this work. First, the mechanical simulations in Section 2.3 suggested that, for devices as big as 300 $\mu$m long, support bridges are not necessary for mechanical stability. Future work could consist of verifying this prediction, and determining the maximum device length required under various conditions, through mechanical stress testing. Provided that the 300 $\mu$m long suspended structures are stable without support bridges, the thermal simulations summarized in Figure 2.16 predict that by removing the support bridges from device 5, its switching power could be reduced by a factor of 2.7. This alone would give a predicted switching power of 35 $\mu$W, with no increase in device footprint. Of course, this would come at the expense of switching times even longer than the switching times of the already slow device 5. Reducing the length of the heater relative to the length of the suspended region is another method of decreasing the switching power that could be explored. Using this method, the heater would only be present in a smaller region in the center of the suspended structure, routed to by a metal that is thicker to ensure low resistance. By increasing the average distance from the heater to the heat sink formed by the substrate, the thermal isolation would be expected to be improved.

The performance of the phase shifters in large switches, like the $4 \times 4$ switch discussed in Chapter 3, should be investigated. Considerations that would be important here include thermal crosstalk between adjacent switches and the effects of any small backscattering introduced by the folded waveguides. A theoretical study of the limits on the optical crosstalk-induced spectral ripple and backscattering for various switch specifications could be useful for determining the maximum waveguide density that can be used for a given application.

For the switches used in this work, the purpose of the optical modelling in Section 2.2 was to guide the design of the folded waveguide structure to achieve the highest waveguide density possible while suppressing crosstalk. Successful design, in this context, results in no coupling of the light between the waveguides and no interesting behaviour in the propagation of the light. The toy model implementing next-to-nearest neighbour coupling for a 3 waveguide structure, however, demonstrated that non-trivial behaviour can be produced using folded waveguides. When more waveguides are present and/or more types of coupling are allowed, for example having both nearest and next-to-nearest neighbour coupling, the behaviour becomes much more complex. A study to search for potential applications of these more complex folded waveguide structures could prove to be worthwhile.

# Bibliography


[1] K. Murray, Z. Lu, H. Jayatilleka, and L. Chrostowski, "Dense dissimilar waveguide routing for highly efficient thermo-optic switches on silicon," Opt. Express **23**, 19575–19585 (2015). → pages iii, iv, 57

[2] Z. Lu, K. Murray, H. Jayatilleka, and L. Chrostowski, "Michelson interferometer thermo-optic switch on SOI with a 50 microwatt power consumption," Photon. Technol. Lett., IEEE pp. 1–1 (2015). → pages iii, iv, 4, 5, 57

[3] L. Chrostowski and M. Hochberg, *Silicon Photonics Design: From Devices to Systems* (Cambridge University Press, 2015). Chap. 4.1. → pages iii, iv, 5, 12, 73, 75

[4] R. Boeck, N. A. F. Jaeger, N. Rouger, and L. Chrostowski, "Series-coupled silicon racetrack resonators and the Vernier effect: theory and measurement," Opt. Express **18**, 25151–25157 (2010). → pages 1

[5] Y. Ding, M. Pu, L. Liu, J. Xu, C. Peucheret, X. Zhang, D. Huang, and H. Ou, "Bandwidth and wavelength-tunable optical bandpass filter based on silicon microring-MZI structure," Opt. Express **19**, 6462–6470 (2011). → pages

[6] A. D Simard and S. LaRochelle, "High performance narrow bandpass filters based on integrated Bragg gratings in silicon-on-insulator," in "Optical Fiber Communication Conference," (Optical Society of America, 2015), pp. Tu3A–2. → pages 1

[7] Y. Hashizume, S. Katayose, T. Tsuchizawa, T. Watanabe, and M. Itoh, "Low-power silicon thermo-optic switch with folded waveguide arms and suspended ridge structures," Electron. Lett. **48**, 1234–1235 (2012). → pages 1, 4

[8] E. Timurdogan, C. M. Sorace-Agaskar, J. Sun, E. S. Hosseini, A. Biberman, and M. R. Watts, "An ultralow power athermal silicon modulator," Nat. Commun. **5** (2014). → pages 1

[9] X. Wang, M. Caverley, J. Flueckiger, Y. Wang, N. A. F. Jaeger, and L. Chrostowski, "Silicon photonic Bragg grating modulators," in "Photonics Conference (IPC), 2014 IEEE," (2014), pp. 190–191. → pages 1

[10] Y. Zhang, S. Yang, Y. Yang, M. Gould, N. Ophir, A. E.-J. Lim, G.-Q. Lo, P. Magill, K. Bergman, T. Baehr-Jones, and M. Hochberg, "A high-responsivity photodetector absent metal-germanium direct contact," Opt. Express **22**, 11367–11375 (2014). → pages 1

[11] J. J. Ackert, D. J. Thomson, L. Shen, A. C. Peacock, P. E. Jessop, G. T. Reed, G. Z. Mashanovich, and A. P. Knights, "High-speed detection at two micrometres with monolithic silicon photodiodes," Nature Photon. **9**, 393–396 (2015). → pages

[12] T. Yin, R. Cohen, M. M. Morse, G. Sarid, Y. Chetrit, D. Rubin, and M. J. Paniccia, "31 GHz Ge n-i-p waveguide photodetectors on silicon-on-insulator substrate," Opt. Express **15**, 13965–13971 (2007). → pages 1

[13] S. T. Fard, K. Murray, M. Caverley, V. Donzella, J. Flueckiger, S. M. Grist, E. Huante-Ceron, S. A. Schmidt, E. Kwok, N. A. F. Jaeger *et al.*, "Silicon-on-insulator sensors using integrated resonance-enhanced defect-mediated photodetectors," Opt. Express **22**, 28517–28529 (2014). → pages 1

[14] A. L. Washburn, L. C. Gunn, and R. C. Bailey, "Label-free quantitation of a cancer biomarker in complex media using silicon photonic microring resonators," Anal. Chem. **81**, 9499–9506 (2009). PMID: 19848413. → pages 1

[15] H. Zhou, C. Li, A. L. Eujin, L. Jia, M. Yu, and G. Lo, "Ultra-compact and broadband Si photonics polarization rotator by self-alignment process," Opt. Express **23**, 6815–6821 (2015). → pages 1

[16] W. D. Sacher, T. Barwicz, B. J. Taylor, and J. K. Poon, "Polarization rotator-splitters in standard active silicon photonics platforms," Opt. Express **22**, 3777–3786 (2014). → pages 1

[17] B. G. Lee, A. V. Rylyakov, W. M. Green, S. Assefa, C. W. Baks, R. Rimolo-Donadio, D. M. Kuchta, M. H. Khater, T. Barwicz, C. Reinholm *et al.*, “Monolithic silicon integration of scaled photonic switch fabrics, CMOS logic, and device driver circuits,” J. Lightw. Technol **32**, 743–751 (2014). → pages 1

[18] A. Alduino, L. Liao, R. Jones, M. Morse, B. Kim, W.-Z. Lo, J. Basak, B. Koch, H.-F. Liu, H. Rong *et al.*, “Demonstration of a high speed 4-channel integrated silicon photonics WDM link with hybrid silicon lasers,” in “Integrated Photonics Research, Silicon and Nanophotonics,” (Optical Society of America, 2010), p. PDIWI5. → pages 1

[19] R. Espinola, M. Tsai, J. Yardley, and J. Osgood, R.M., “Fast and low-power thermooptic switch on thin silicon-on-insulator,” Photon. Technol. Lett., IEEE **15**, 1366–1368 (2003). → pages 1, 2

[20] L. Shang, L.-S. Peh, A. Kumar, and N. K. Jha, “Thermal modeling, characterization and management of on-chip networks,” in “Proceedings of the 37th annual IEEE/ACM International Symposium on Microarchitecture,” (IEEE Computer Society, 2004), pp. 67–78. → pages 1

[21] J. Xia, J. Yu, Z. Fan, Z. Wang, and S. Chen, “Thermo-optic variable optical attenuator with low power consumption fabricated on silicon-on-insulator by anisotropic chemical etching,” Opt. Eng. **43**, 789–790 (2004). → pages 2

[22] T. Chu, H. Yamada, S. Ishida, and Y. Arakawa, “Thermooptic switch based on photonic-crystal line-defect waveguides,” Photon. Technol. Lett., IEEE **17**, 2083–2085 (2005). → pages 2

[23] J. Song, Q. Fang, S. H. Tao, T. Y. Liow, M. B. Yu, G. Q. Lo, and D. L. Kwong, “Fast and low power Michelson interferometer thermo-optical switch on SOI,” Opt. Express **16**, 15304–15311 (2008). → pages 2, 57

[24] Y. Vlasov, W. M. Green, and F. Xia, “High-throughput silicon nanophotonic wavelength-insensitive switch for on-chip optical networks,” Nature Photon. **2**, 242–246 (2008). → pages 2

[25] P. Dong, S. F. Preble, and M. Lipson, “All-optical compact silicon comb switch,” Opt. Express **15**, 9600–9605 (2007). → pages 2

[26] T. Chu, H. Yamada, S. Ishida, and Y. Arakawa, “Compact 1 $\times$ N thermo-optic switches based on silicon photonic wire waveguides,” Opt. Express **13**, 10109–10114 (2005). → pages 2

[27] L. Sanchez, A. Griol, S. Lechago, A. Brimont, and P. Sanchis, "Low-Power Operation in a Silicon Switch Based on an Asymmetric Mach-Zehnder Interferometer," Photon. J, IEEE **7**, 1–8 (2015). → pages 2

[28] P. Dong, L. Chen, and Y. kai Chen, "High-speed low-voltage single-drive push-pull silicon Mach-Zehnder modulators," Opt. Express **20**, 6163–6169 (2012). → pages 2

[29] G. Kim, I. G. Kim, S. Kim, J. Joo, K.-S. Jang, S. A. Kim, J. H. Oh, J. W. Park, M.-J. Kwack, J. Park, H. Park, G. S. Park, and S. Kim, "Silicon photonic devices based on SOI/bulk-silicon platforms for chip-level optical interconnects," Proc. SPIE **9368**, 93680Z–93680Z–7 (2015). → pages 2

[30] P. Dong, W. Qian, H. Liang, R. Shafiiha, D. Feng, G. Li, J. E. Cunningham, A. V. Krishnamoorthy, and M. Asghari, "Thermally tunable silicon racetrack resonators with ultralow tuning power," Opt. Express **18**, 20298–20304 (2010). → pages 2

[31] R. A. Soref and B. Bennett, "Electrooptical effects in silicon," J. Quantum Electron., IEEE **23**, 123–129 (1987). → pages 2

[32] G. Cocorullo, F. G. Della Corte, and I. Rendina, "Temperature dependence of the thermo-optic coefficient in crystalline silicon between room temperature and 550 K at the wavelength of 1523 nm," Appl. Phys. Lett. **74**, 3338–3340 (1999). → pages 2

[33] Y. Shoji, K. Kintaka, S. Suda, H. Kawashima, T. Hasama, and H. Ishikawa, "Low-crosstalk $2 \times 2$ thermo-optic switch with silicon wire waveguides," Opt. Express **18**, 9071–9075 (2010). → pages 2

[34] M. R. Watts, J. Sun, C. DeRose, D. C. Trotter, R. W. Young, and G. N. Nielson, "Adiabatic thermo-optic Mach-Zehnder switch," Opt. Lett. **38**, 733–735 (2013). → pages 2, 40

[35] Y. Akihama and K. Hane, "Single and multiple optical switches that use freestanding silicon nanowire waveguide couplers," Light Sci. Appl. **1**, e16 (2012). → pages 2

[36] K. Murray and L. Chrostowski, "Modeling optical switching by electrostatic deformaion of suspended silion waveguides," in "Optical MEMS and Nanophotonics (OMN), 2014 International Conference on," (2014), pp. 113–114. → pages 2

[37] J. Walraven, “Failure mechanisms in MEMS,” in “Test Conference, 2003. Proceedings. ITC 2003. International,” , vol. 1 (2003), vol. 1, pp. 828–833. → pages 2, 28

[38] Y. Akihama, Y. Kanamori, and K. Hane, “Ultra-small silicon waveguide coupler switch using gap-variable mechanism,” Opt. Express **19**, 23658–23663 (2011). → pages 2

[39] E. Bulgan, Y. Kanamori, and K. Hane, “Submicron silicon waveguide optical switch driven by microelectromechanical actuator,” Appl. Phys. Lett. **92**, 101110 (2008). → pages 2

[40] S. Han, T. J. Seok, N. Quack, B.-w. Yoo, and M. C. Wu, “Monolithic 50×50 MEMS silicon photonic switches with microsecond response time,” in “Optical Fiber Communication Conference,” (Optical Society of America, 2014), p. M2K. → pages 2

[41] M. W. Geis, S. J. Spector, R. Williamson, and T. Lyszczarz, “Submicrosecond submilliwatt silicon-on-insulator thermooptic switch,” Photon. Technol. Lett., IEEE **16**, 2514–2516 (2004). → pages 4

[42] N. C. Harris, Y. Ma, J. Mower, T. Baehr-Jones, D. Englund, M. Hochberg, and C. Galland, “Efficient, compact and low loss thermo-optic phase shifter in silicon,” Opt. Express **22**, 10487–10493 (2014). → pages 4

[43] Q. Fang, J. F. Song, T.-Y. Liow, H. Cai, M. B. Yu, G.-Q. Lo, and D.-L. Kwong, “Ultralow power silicon photonics thermo-optic switch with suspended phase arms,” Photon. Technol. Lett, IEEE **23**, 525–527 (2011). → pages 4, 31

[44] R. Kasahara, K. Watanabe, M. Itoh, Y. Inoue, and A. Kaneko, “Extremely low power consumption thermooptic switch (0.6 mW) with suspended ridge and silicon-silica hybrid waveguide structures,” in “Optical Communication, 2008. ECOC 2008. 34th European Conference on,” (2008), pp. 1–2. → pages

[45] P. Sun and R. M. Reano, “Submilliwatt thermo-optic switches using free-standing silicon-on-insulator strip waveguides,” Opt. Express **18**, 8406–8411 (2010). → pages 4

[46] A. Densmore, S. Janz, R. Ma, J. H. Schmid, D.-X. Xu, A. Delâge, J. Lapointe, M. Vachon, and P. Cheben, “Compact and low power thermo-optic switch using folded silicon waveguides,” Opt. Express **17**, 10457–10465 (2009). → pages 4

[47] A. Yariv, “Coupled-mode theory for guided-wave optics,” J. Quantum Electron., IEEE **9**, 919–933 (1973). → pages 4

[48] W.-P. Huang, “Coupled-mode theory for optical waveguides: an overview,” J. Opt. Soc. Am. A **11**, 963–983 (1994). → pages 5, 10, 12

[49] V. Donzella, S. Talebi Fard, and L. Chrostowski, “Study of waveguide crosstalk in silicon photonics integrated circuits,” Proc. SPIE 8915, Photonics North 2013 p. 89150Z (2013). → pages 5

[50] W. Song, R. Gatdula, S. Abbaslou, M. Lu, A. Stein, W. Y.-C. Lai, J. Provine, R. F. W. Pease, D. N. Christodoulides, and W. Jiang, “High-density waveguide superlattices with low crosstalk,” Nat. Commun. **6** (2015). → pages 5, 45

[51] L. Liu, “Densely packed waveguide array (DPWA) on a silicon chip for mode division multiplexing,” Opt. Express **23**, 12135–12143 (2015). → pages 5

[52] M. Mrejen, H. Suchowski, H. Taiki, W. Chihhui, F. Liang, O. Kevin, Y. Wang, and X. Zhang, “Adiabatic elimination-based coupling control in densely packed subwavelength waveguides,” Nat. Commun. **6** (2015). → pages 5, 27

[53] H. Yun, W. Shi, Y. Wang, L. Chrostowski, and N. A. F. Jaeger, “2×2 adiabatic 3-dB coupler on silicon-on-insulator rib waveguides,” Proc. SPIE, Photonics North 2013 **8915**, 89150V (2013). → pages 7, 42, 49

[54] W. Bogaerts, P. De Heyn, T. Van Vaerenbergh, K. De Vos, S. Kumar Selvaraja, T. Claes, P. Dumon, P. Bienstman, D. Van Thourhout, and R. Baets, “Silicon microring resonators,” Laser Photon. Rev. **6**, 47–73 (2012). → pages 19

[55] J. Sakurai and J. Napolitano, *Modern Quantum Mechanics* (Pearson Education, 2014). → pages 21

[56] J. Zinn-Justin, *Path Integrals in Quantum Mechanics*, Oxford Graduate Texts (OUP Oxford, 2010). → pages 21

[57] D. Griffiths, *Introduction to Quantum Mechanics*, Pearson international edition (Pearson Prentice Hall, 2005). → pages 21, 27

[58] L. Pauling and E. Wilson, *Introduction to Quantum Mechanics: With Applications to Chemistry*, Dover Books on Physics (Dover Publications, 1985). → pages 21

[59] M. Peskin and D. Schroeder, *An Introduction to Quantum Field Theory*, Advanced book classics (Addison-Wesley Publishing Company, 1995). → pages 21

[60] A. Zee, *Quantum Field Theory in a Nutshell: (Second Edition)* (Princeton University Press, 2010). → pages

[61] M. Srednicki, *Quantum Field Theory* (Cambridge University Press, 2007). → pages 21

[62] E. Gozzi, M. Reuter, and W. D. Thacker, "Hidden BRS invariance in classical mechanics. II," Phys. Rev. D **40**, 3363–3377 (1989). → pages 21

[63] A. Wipf, *Statistical Approach to Quantum Field Theory: An Introduction* (Springer Berlin Heidelberg, 2012). → pages 21

[64] R. P. Feynman, "Space-time approach to quantum electrodynamics," Phys. Rev. **76**, 769–789 (1949). → pages 21

[65] F. Pedrotti, L. Pedrotti, and L. Pedrotti, *Introduction to Optics* (Pearson Prentice Hall, 2007). → pages 26

[66] S. Longhi, "Adiabatic passage of light in coupled optical waveguides," Phys. Rev. E **73**, 026607 (2006). → pages 27

[67] R. Khomeriki and S. Ruffo, "Nonadiabatic Landau-Zener tunneling in waveguide arrays with a step in the refractive index," Phys. Rev. Lett. **94**, 113904 (2005). → pages 27

[68] J. Cai, Y. Ishikawa, and K. Wada, "Strain induced bandgap and refractive index variation of silicon," Opt. Express **21**, 7162–7170 (2013). → pages 28

[69] N. Bansal and R. Doremus, *Handbook of Glass Properties*, Academic Press handbook series (Elsevier Science, 2013). → pages 31

[70] J. Lienhard, *A Heat Transfer Textbook*, Dover Books on Engineering (Dover Publications, 2011). → pages 33, 37, 39, 76

[71] M. Yang, W. M. J. Green, S. Assefa, J. V. Campenhout, B. G. Lee, C. V. Jahnes, F. E. Doany, C. L. Schow, J. A. Kash, and Y. A. Vlasov, "Non-blocking 4x4 electro-optic silicon switch for on-chip photonic networks," Opt. Express **19**, 47–54 (2011). → pages 45

[72] Y. Zhang, S. Yang, A.-J. Lim, G.-Q. Lo, C. Galland, T. Baehr-Jones, and M. Hochberg, “A CMOS-compatible, low-loss, and low-crosstalk silicon waveguide crossing,” Photon. Technol. Lett., IEEE **25**, 422–425 (2013). → pages 46

[73] Y. Wang, J. Flueckiger, C. Lin, and L. Chrostowski, “Universal grating coupler design,” Proc. SPIE **8915**, 89150Y–89150Y–7 (2013). → pages 46, 50

[74] L. Chrostowski, X. Wang, J. Flueckiger, Y. Wu, Y. Wang, and S. T. Fard, “Impact of fabrication non-uniformity on chip-scale silicon photonic integrated circuits,” in “Optical Fiber Communication Conference,” (Optical Society of America, 2014), p. Th2A.37. → pages 50

[75] H. Wei, J. Yu, X. Zhang, and Z. Liu, “Compact 3-dB tapered multimode interference coupler in silicon-on-insulator,” Opt. Lett. **26**, 878–880 (2001). → pages 60

# Appendix A

# Path Integral Approach for a Directional Coupler

Consider a directional coupler composed of two identical, parallel waveguides that are sufficiently small so as the directional coupler supports only two eigenmodes, $|1\rangle$ and $|2\rangle$ with propagation constants $k_1$ and $k_2$, respectively, as in Section 2.2. Define the single waveguide modes $|\bar{A}\rangle$ and $|\bar{B}\rangle$ in the same manner as in Section 2.2. If the waveguides are weakly coupled then modal expansion gives [3]

$$|\bar{A}\rangle \;=\; (|1\rangle + |2\rangle)/\sqrt{2} \tag{A.1}$$

and

$$|\bar{B}\rangle \;=\; (|1\rangle - |2\rangle)/\sqrt{2}. \tag{A.2}$$

Suppose that such a directional coupler, of length $L$, is initially excited in the state $|\bar{A}\rangle$ and the field amplitude of mode $|\bar{A}\rangle$ at the directional coupler output is measured. That is, we are interested in the quantity

$$\langle\bar{A}|\, e^{iPL}\, |\bar{A}\rangle, \tag{A.3}$$

where here the momentum operator $P$ is defined in the basis-independent way

$$\frac{\mathrm{d}\,|\psi\rangle}{\mathrm{d}z} = iP\,|\psi\rangle, \tag{A.4}$$

where $z$ is the propagation distance and $|\psi\rangle$ is any state. Rewriting the exponential in the expression A.3

$$\langle\bar{A}|\, e^{iPL/M}...e^{iPL/M}\,|\bar{A}\rangle\,, \tag{A.5}$$

where there are $M$ products of the exponential, can be interpreted as successively propagating over the directional coupler broken down into $M$ subsections. Assuming that the structure is lossless, the radiation modes can be ignored and the set $\{|\bar{A}\rangle\,, |\bar{B}\rangle\}$ is a complete, orthonormal set. Thus, the unit operator can be written as the following projection operator:

$$1 = \sum_{n=\bar{A},\bar{B}} |n\rangle\,\langle n|\,. \tag{A.6}$$

Introducing the unit operator $M+1$ times into the expression A.5 gives the following expression:

$$\sum_{n_1,n_2,...n_{M+1}=\bar{A},\bar{B}} \langle\bar{A}|n_{M+1}\rangle\,\langle n_{M+1}|\, e^{iPL/M}\,|n_M\rangle\,\langle n_M|\,...\,|n_2\rangle\,\langle n_2|\, e^{iPL/M}\,|n_1\rangle\,\langle n_1|\bar{A}\rangle\,. \tag{A.7}$$

The expression A.7 is the path integral approach for a directional coupler. For each set of the dummy indices, $\{n_1, n_2, ...n_m\}$, the term in the expression A.7 contains the product of $M$ through or cross-coupling coefficients, $\langle n_{j+1}|\, e^{iPL/M}\,|n_j\rangle$, giving a path through the directional coupler. The coefficient is a through coupling coefficient if $n_{j+1} = n_j$ and a cross-coupling coefficient otherwise. Further, the sum is over all sets of dummy indices, so every possible path contributes to the transmission amplitude. Since the expression A.7 is equivalent to the expression A.3 for arbitrary $M$, the limit as $M \to \infty$ exists and is equal to A.3.

One can convert the expression A.7 to the coupled mode formalism to show that they are equivalent by noting that the set $\{|1\rangle\,, |2\rangle\}$ is also an orthonormal set that can be used to write down the unit operator. Rewriting the expression A.7 using this unit operator gives

$$\sum_{n_1,n_2,...n_{M+1}=1,2} \langle\bar{A}|n_{M+1}\rangle\,\langle n_{M+1}|\, e^{iPL/M}\,|n_M\rangle\,\langle n_M|\,...\,|n_2\rangle\,\langle n_2|\, e^{iPL/M}\,|n_1\rangle\,\langle n_1|\bar{A}\rangle\,. \tag{A.8}$$

Using the fact that $|1\rangle$ and $|2\rangle$ are the eigenmodes of the momentum operator with eigenvalues $k_1$ and $k_2$, and that they are orthonormal simplifies expression A.8 considerably.

$$\sum_{n_1=1,2} \langle \bar{A} | n_1 \rangle e^{ik_{n_1}L} \langle n_1 | \bar{A} \rangle \tag{A.9}$$

That is, the amplitude of mode $|\bar{A}\rangle$ at the output can be obtained by decomposing the input mode into a sum of the two eigenmodes, propagating the eigenmodes independently, and then projecting onto $|\bar{A}\rangle$. Utilizing the mode decomposition equation A.1 gives

$$\frac{1}{2}\left(e^{ik_1L} + e^{ik_2L}\right). \tag{A.10}$$

The normalized transmission is then given as

$$\left|\frac{1}{2}\left(e^{ik_1L} + e^{ik_2L}\right)\right|^2 = \frac{1}{2}\left(1 + \cos\left[(k_1 - k_2)L\right]\right). \tag{A.11}$$

This is, of course, the usual result [3].

# Appendix B

# A Lower Bound for Switch Figure of Merit

To compute a lower bound on a silicon switch figure of merit, here we compute the figure of merit for a silicon wire waveguide phase shifter suspended only by its ends in vacuum and uniformly heated with a total power $P$. Since all of the power supplied to the phase shifter goes towards heating the silicon, this geometry represents a maximum heating efficiency and should result in a lower bound on the figure of merit.

Consider a straight silicon waveguide with cross-sectional area, $A$, length, $L$, specific heat, $c$, density, $\rho$, and thermal conductivity, $K$. Furthermore, assume that the waveguide is long enough such that the temperature change corresponding to a $\pi$ phase shift is small enough to ignore thermal radiation losses. Denoting the power supplied per unit volume as $Q = P/AL$, the temperature distribution, $T$, satisfies the heat equation with a source [70]

$$\frac{\partial T}{\partial t} = \frac{K}{c\rho}\frac{\partial^2 T}{\partial x^2} + \frac{Q}{c\rho}. \tag{B.1}$$

Considering the steady state solution, $\frac{\partial T}{\partial t} = 0$, and imposing the condition that the temperature at the ends of the waveguide, $x = \pm L/2$, is 0, we get the solution

$$T = \frac{Q}{2K}\left(L^2/4 - x^2\right), \tag{B.2}$$

and the average temperature change

$$\bar{T} = \frac{PL}{12AK}. \tag{B.3}$$

Thus, by equation 2.32, the switching power is

$$P_\pi = \frac{6AK\lambda}{L^2 \mathrm{d}n_{\mathrm{eff}}/\mathrm{d}T}. \tag{B.4}$$

To calculate the characteristic response time of the device we can solve the time dependent source free heat equation and determine the fall time constant. The heat equation then reads

$$\frac{\partial T}{\partial t} = \frac{K}{c\rho}\frac{\partial^2 T}{\partial x^2}. \tag{B.5}$$

Assuming that the solution is separable, $T(x,t) = X(x)A(t)$, we get

$$\frac{X''}{X} = \frac{c\rho}{K}\frac{A'}{A} = -\gamma, \tag{B.6}$$

where $\gamma$ is a constant of separation. The lowest order non-zero solution satisfying the boundary conditions $X(\pm L/2) = 0$ has $\gamma = \pi^2/L^2$ and so

$$\frac{A'}{A} = -\frac{K\pi^2}{c\rho L^2}, \tag{B.7}$$

corresponding to a time constant of $\tau_c = c\rho L^2/\pi^2 K$. Finally, we have an expression for the phase shifter figure of merit

$$P_\pi \tau_c = \frac{6Ac\rho\lambda}{\pi^2 \mathrm{d}n_{\mathrm{eff}}/\mathrm{d}T}. \tag{B.8}$$

For a silicon waveguide with cross-section 500 nm$\times$220 nm this gives a figure of merit of approximately 0.88 nJ at 1550 nm.